Remote Sensing of Environment 257 (2021) 112344

Contents lists available at ScienceDirect

Remote Sensing of Environment

journal homepage: www.elsevier.com/locate/rse

Validation and analysis of Terra and Aqua MODIS, and SNPP VIIRS vegetation indices under zero vegetation conditions: A case study using Railroad Valley Playa

Tomoaki Miura [a,*], Charlotte Z. Smith [a], Hiroki Yoshioka [b]

[a] Department of Natural Resources and Environmental Management, University of Hawaii at Manoa, Honolulu 96822, USA
[b] Department of Information Science and Technology, Aichi Prefectural University, Nagakute, Aichi 480-1198, Japan

ARTICLE INFO

Editor: Jing M. Chen

Keywords:
Terra MODIS
Aqua MODIS
VIIRS
NDVI
EVI
EVI2
Soils
Soil line
Railroad Valley Playa
RadCaTS
Validation
Performance evaluation

ABSTRACT

Spectral vegetation index (VI) time series data from coarse resolution satellite sensors, such as the Moderate Resolution Imaging Spectroradiometer (MODIS), have been utilized in studying vegetation dynamics. Numerous studies have evaluated how well VI products capture variations in vegetation biophysical or physiological conditions. Equally important is to evaluate VI products over "zero vegetation" surfaces consisting of soils, litters, and/or rocks, as they define the lower bound for vegetation detection. VIs, however, vary over zero vegetation surfaces as a function of soil moisture content and surface roughness. In this study, we evaluated the behavior of VIs from Terra MODIS (T-MODIS), Aqua MODIS (A-MODIS), and Suomi-National Polar-orbiting Partnership Visible Infrared Imaging Radiometer Suite (S-VIIRS) at Railroad Valley Playa, Nevada for a period from April 2013 to September 2019. The playa is a dried lakebed devoid of vegetation throughout the year. Long-term *in situ* reflectance measurements acquired over the 1 km-by−1 km Radiometric Calibration Test Site (RadCaTS) located on the playa were obtained from the Radiometric Calibration Network (RadCalNet) portal and used as a reference. Three VIs were analyzed, including the normalized difference VI (NDVI), enhanced VI (EVI), and two-band EVI (EVI2). RadCaTS NDVI, EVI, and EVI2 of the playa surface increased and decreased occasionally for the time period examined in this study, and the satellite NDVIs, EVIs, and EVI2s had comparable temporal signatures to the RadCaTS counterparts. T-MODIS and A-MODIS NDVI and EVI2 values were comparable to the RadCaTS counterparts, whereas T-MODIS and A-MODIS EVI values were lower than the RadCaTS counterparts by ~0.006 and ~ 0.01 EVI units, respectively. All the three VIs of S-VIIRS were consistently higher than their RadCaTS counterparts by ~0.008 VI units, due to the higher near-infrared (NIR) reflectances of S-VIIRS than the RadCaTS NIR reflectance. The red and NIR, and red and blue reflectances each formed linear relationships (*i.e.*, soil lines) for each of the three sensors. Variations in reflectance due to surface conditions and observation geometries all appeared as variations along these soil lines. The satellite red-NIR soil lines were comparable to the RadCaTS counterparts, whereas the satellite red-blue soil lines had steeper slopes than the RadCaTS counterparts due to a negative bias in the satellite blue reflectances. This translated into the T-MODIS and A-MODIS EVI behaviors different from those depicted by RadCaTS EVI, and the satellite NDVI and EVI2 behaving more comparably with the RadCaTS counterparts and across the three sensors than the satellite EVI.

Objectives of the work

- To evaluate how well MODIS and VIIRS vegetation indices (VIs) compared with *in situ* measured VIs in terms of seasonal/inter-annual variations and actual VI values for zero vegetation conditions
- To determine the expected VI values and their variability due to a range of surface conditions and sun/view angles

Background: Spectral VIs are one of more important satellite products in studying vegetation seasonal changes and inter-annual variability. Numerous studies have been conducted to validate and evaluate VI products over various vegetated surfaces, or VI sensitivity to variations in vegetation biophysical/physiological conditions. To the knowledge of the authors, there have been no studies that validated VI products over "zero vegetation" surfaces across seasons for multiple

* Corresponding author.
E-mail address: tomoakim@hawaii.edu (T. Miura).

https://doi.org/10.1016/j.rse.2021.112344
Received 31 July 2020; Received in revised form 31 December 2020; Accepted 5 February 2021
Available online 19 February 2021

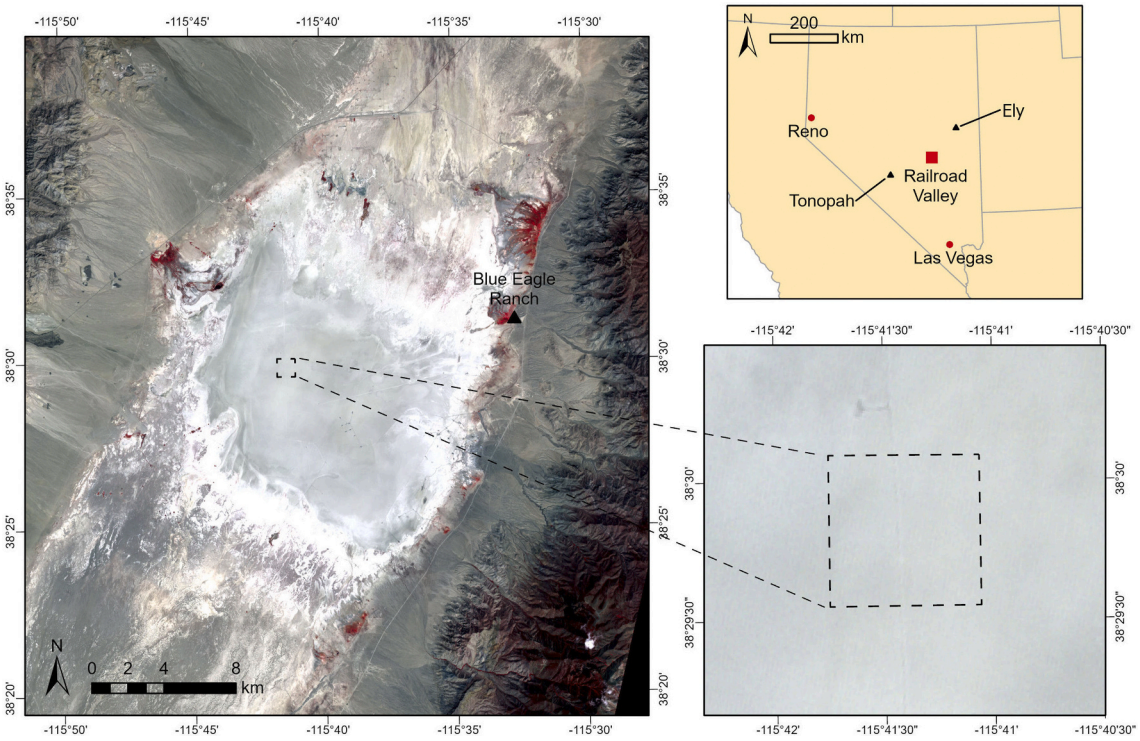

Fig. 1. Map of study area, Railroad Valley Playa, Nevada (left). The squares on the left and lower-right frames indicate the 1 km-by−1 km Radiometric Calibration Test Site (RadCaTS) area. The left frame also indicates the location of the Blue Eagle Ranch weather station. The false-colour image used on the left and lower-right frames is an image acquired with the Terra ASTER (Advanced Spaceborne Thermal Emission and Reflection Radiometer) sensor on 1 September 2018. (For interpretation of the references to colour in this figure legend, the reader is referred to the web version of this article.)

years using *in situ* measurements as a reference. As multi-year, continuous field reflectance data over Railraod Valley Playa became recently available, we conducted this case study.

1. Introduction

Spectral vegetation index (VI) time series data from coarse resolution satellite sensors, such as the National Oceanic and Atmospheric Administration (NOAA) Advanced Very High Resolution Radiometer (AVHRR) and the National Aeronautics and Space Administration (NASA) Moderate Resolution Imaging Spectroradiometer (MODIS), have been utilized in various studies that involve vegetation dynamics, including ecosystem sensitivity analysis to climate variability, greening trend analysis, and drought assessment (Seddon et al., 2016; Zhang et al., 2017; Lu et al., 2019). Recently, medium spatial resolution VI time series data derived from the Landsat series or harmonized Landsat-8 and Sentinel-2 datasets were used to characterize vegetation phenology and land use dynamics in much finer spatial detail than what could be accomplished with coarse resolution satellite data (Zhu et al., 2016; Bolton et al., 2020; Liu et al., 2020). Yet, another set of studies investigated the utility of hyper-temporal VI time series data derived from new-generation geostationary satellites such as the Advanced Himawari Imager (AHI), and Spinning Enhanced Visible and Infrared Imager (SEVIRI) for detecting vegetation seasonal changes and their inter-annual variability with higher accuracies than those derived from MODIS or Suomi-National Polar-orbiting Partnership (S-NPP) Visible Infrared Imaging Spectroradiometer Suite (VIIRS) (Barbosa et al., 2019; Miura et al., 2019; Yan et al., 2019).

VIs are spectral transformations of multi-band reflectances, often involving the red and near-infrared (NIR) bands, designed to extract and enhance the signal contribution from green vegetation. They measure "vegetation greenness," a composite property of leaf chlorophyll, leaf area, canopy cover, and canopy architecture (Jiang et al., 2008). Numerous studies have evaluated the behavior of VIs both theoretically and empirically, and validated satellite VI products to determine how well VIs capture seasonal changes and variations in vegetation biophysical or physiological conditions (*e.g.*, Yan et al., 2016; Cho and Ramoelo, 2019; Badgley et al., 2017; Shi et al., 2017). In these studies, VI temporal profiles from MODIS, AVHRR, and Medium Resolution Imaging Spectrometer (MERIS), for example, were cross-compared with those of *in situ* VIs derived from time-lapse cameras, radiation flux measurements, or tower-mounted spectrometers (Cheng et al., 2006; Muraoka et al., 2013; Rankine et al., 2017), leaf area index (LAI) (Qiao et al., 2020), gross primary productivity (GPP), (Wang et al., 2004; Olofsson et al., 2008; Huete et al., 2002), fraction of absorbed photosynthetically-active radiation (fAPAR) (Fensholt et al., 2004; Gitelson et al., 2014), and phenology observations (Liang et al., 2011; Liang et al., 2014).

As equally important as evaluating VI sensitivity to vegetation greenness and biophysical parameters is to evaluate VI behavior over "zero vegetation" surfaces consisting of soils, litters, and/or rocks. VI values for zero vegetation define the lower bound below which photosynthetically-active vegetation is considered non-existent. In other words, any positive deviations from this baseline are considered the contributions from green vegetation. However, VIs over zero vegetation surfaces have been known to vary as a function of soil type, soil moisture content, soil organic matter content, and surface roughness, resulting in errors/uncertainties of VI-based detection and quantification of green vegetation (Montandon and Small, 2008; Yoshioka et al., 2010).

VI behavior and variability for zero vegetation conditions, or bare soils, have been investigated from two perspectives. One perspective is for the estimation of fractional vegetation cover (FVC) with the normalized difference vegetation index (NDVI) where best VI values for bare soils were obtained as a statistical moment of multi-year NDVI time series image data (Gutman and Ignatov, 1998; Zeng et al., 2000; Ichii et al., 2001; Matsui et al., 2005). The other perspective has focused on

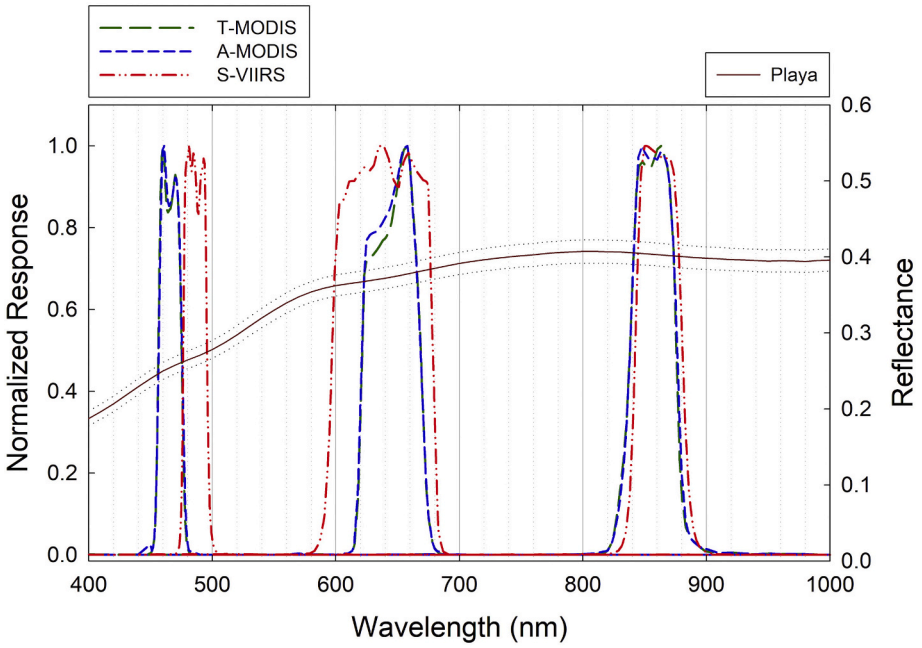

Fig. 2. Typical hyperspectral reflectance of the Radiometric Calibration Test Site (RadCaTS) on Railroad Valley Playa plotted along with the normalized spectral responses of Terra MODIS (T-MODIS), Aqua MODIS (A-MODIS), and Suomi-NPP VIIRS (S-VIIRS) red, NIR, and blue bands. The hyperspectral reflectance was acquired at 12:00 pm PST (Pacific Standard Time) on 1 June 2016. The dotted lines above and below the playa spectral reflectance are their standard uncertainties. (For interpretation of the references to colour in this figure legend, the reader is referred to the web version of this article.)

characterizing variations in actual soil reflectances. Red and NIR reflectances of soils have been known to form a linear relationship in the reflectance space, called the "soil line" concept (Huete, 1989; Baret et al., 1993). Variations of soil lines have been used as a means to examine the influences of soil reflectance variations on VIs (Galvão and Vitorello, 1998; Yoshioka et al., 2010). These studies with two different perspectives have come to suggest the need of spatially-varying VI values for zero vegetation conditions in order to reduce the errors/uncertainties of VI-based vegetation detection (Baret et al., 1993; Fox et al., 2004; Montandon and Small, 2008; Wu et al., 2014). Nearly all of these studies were conducted solely with model-simulated data, numerical analysis, laboratory-measured spectral data, or satellite image data.

In this study, we evaluated MODIS and VIIRS VIs under zero vegetation conditions using Railroad Valley Playa, Nevada as a study site. The playa is a dried lakebed devoid of vegetation throughout the year. Long-term *in situ* reflectance and atmospheric measurements have been made continuously since the year 2013 on the playa (Czapla-Myers et al., 2016). This dataset has recently been made available to the public *via* the Radiometric Calibration Network (RadCalNet) (Bouvet et al., 2019). The long-term, continuous nature of the dataset allows for comparisons with MODIS and VIIRS VI data throughout seasons across multiple years for a zero vegetation surface. A primary objective of this study was to evaluate how well MODIS and VIIRS VIs compared with *in situ* measured VIs in terms of seasonal/inter-annual variations and actual VI values. MODIS and VIIRS reflectances were also compared with the *in situ* reflectances from the same perspectives. This analysis was conducted on nadir/near-nadir observations as the *in situ* measurements were made with nadir viewing geometry. MODIS and VIIRS VI products can include observations made from a wide range of view zenith angles as these widely-used products are not normalized to a standard geometry with a bi-directional reflectance distribution function (BRDF)-correction model. Off-nadir VI values would likely be different from their nadir counterparts as directional reflectances of soils vary with the position of the Sun and observer (Irons et al., 1992; Wang et al., 2014). Thus, our secondary objective was to examine how different off-nadir VI values were from their nadir values and how much additional variation off-nadir VIs introduced to that observed on nadir VIs in the above. To the knowledge of the authors, this is the first study that validated MODIS and VIIRS VI products and quantified their variability over zero vegetation surfaces using *in situ* measurements as a reference across seasons for multiple years.

2. Railroad Valley Playa and Radiometric Calibration Test Site (RadCaTS)

Railroad Valley (RRV) Playa, Nevada is a flat, dried lakebed devoid of vegetation all year around (Fig. 1). It is located approximately between the two towns of Tonopah, Nevada and Ely, Nevada, and under the United States Bureau of Land Management stewardship. The mean annual precipitation measured at the two nearest long-term weather stations of Tonopah and Ely are 130 mm and 250 mm, respectively (based on 1981–2010 data) (Czapla-Myers, 2018).

The playa is a well-established site for the vicarious calibration of solar-reflective spectral bands of various satellite sensors, including Terra MODIS (T-MODIS), Aqua MODIS (A-MODIS), and S-NPP VIIRS (S-VIIRS) (Czapla-Myers et al., 2017). The playa has also been used for long-term stability monitoring of Earth Observing-One Hyperion (Campbell et al., 2013), and cross-calibration across the Landsat series (Teillet et al., 2006; Teillet et al., 2007) and between the Advanced Spaceborne Thermal Emission Reflection Radiometer (ASTER) and Terra MODIS visible to near-infrared (NIR) bands (Obata et al., 2017). Likewise, it has been used to evaluate AERONET-based surface reflectance validation network (ASRVN) (Wang et al., 2011) and the surface reflectance products derived from T-MODIS, MERIS, Terra Multi-angle Imaging Spectroradiometer (MISR), and Landsat-7 Enhanced Thematic Mapper Plus (ETM+) with those acquired with a multi-angular and multi-spectral airborne radiometer instrument, the Cloud Absorption Radiometer (CAR) as a reference (Kharbouche et al., 2017). Yates et al. (2013) used the playa to study carbon fluxes of soils under no vegetation.

Optically, the playa is characterized with its high surface reflectance (Fig. 2), but the reflectance is known to fluctuate across seasons due primarily to the moisture content of the surface (Czapla-Myers et al., 2008). Bruegge et al. (2019) reported that the surface reflectance stabilized after approximately 1–2 weeks of dry conditions. As the surface dries out, a white crust often forms on the surface and increase the surface reflectance (Czapla-Myers et al., 2008). The crust is not uniformly distributed on the playa (Czapla-Myers et al., 2007). The playa surface typically has cracks due to shrink-swell clays composing the surface.

Bruegge et al. (2019) characterized the BRDF of the playa surface reflectance with a number of datasets acquired with field instruments such as the Portable Apparatus for Rapid Acquisition of Bidirectional Observation of the Land and Atmosphere (PARABOLA), and the MISR and MODIS sensors. They found that the off-nadir correction factor, which is the ratio of bi-directional reflectance factor (BRF) at a given view zenith and azimuth angles to the nadir-view BRF at the same sun position, is consistent in time and space for view zenith angles as large as 30°, and spectrally invariant.

In this study, we used *in situ* surface reflectance time series measurements from the Radiometric Calibration Test Site (RadCaTS) maintained by the University of Arizona Remote Sensing Group as a reference. The RadCaTS site is a 1 km-by−1 km area delineated on Railroad Valley Playa (38.497°N, 115.690°W, 1435 m above mean sea level) (Fig. 1). The RadCaTS facility is a suite of instruments to make *in situ* measurements of the surface and atmosphere to predict the "top-of-atmosphere (TOA)" spectral radiance reflected from the earth's surface during daytime, clear-sky conditions (Czapla-Myers et al., 2016). RadCaTS is one of four sites that constitute the RadCalNet managed by the the Committee on Earth Observation Satellites (CEOS) Working Group on Calibration and Validation (WGCV) (Bouvet et al., 2019).

RadCaTS data products have been made available *via* the RadCalNet portal (Bouvet et al., 2019). The products include hyperspectral "bottom-of-atmosphere (BOA)" reflectance and hyperspectral TOA radiance (400–2500 nm at 10 nm sampling intervals) representing the 1 km-by−1 km area at 30 min intervals from 9:00 to 15:00 Pacific Standard Time (PST). The site is viewed with four multi-band ground-viewing radiometers (GVRs) of which locations were carefully chosen to represent the surface reflectance of the 1 km-by−1 km area (Czapla-Myers et al., 2007). To obtain a hyperspectral reflectance for a given date and time, the four GVR's reflected radiance measurements are averaged and converted into multi-band surface reflectances using incoming surface irradiances predicted with the MODTRAN radiative transfer code constrained with *in situ* and satellite atmospheric measurements. A hyperspectral surface reflectance is selected from a database of *in situ* hyperspectral datasets that best-matches the GVR's multi-band surface reflectances. Czapla-Myers et al. (2016) describes the algorithm used to obtain RadCaTS hyperspectral surface reflectances in detail.

According to Czapla-Myers and Woolliams (2018), the sources of uncertainty associated with the surface reflectance are the uncertainties associated with the GVR measurements, MODTRAN radiative transfer model, *exo*-atmospheric solar irradiance, and picking of hyperspectral reflectance from the database. The combined, standard uncertainty of a surface reflectance ranges from 3.6% to 5.3%, depending on the wavelengths, but about 5% on average (Czapla-Myers and Woolliams, 2018).

3. Materials and methods

3.1. RadCaTS data

RadCaTS hyperspectral BOA reflectance data (Input Version 4) were downloaded from the RadCalNet portal (Bouvet et al., 2019). The downloaded data covered a period from 1 April 2013 to 20 September 2019. The surface reflectances were band-averaged to represent T- and A-MODIS, and S-VIIRS bandpass reflectances for the red, NIR, and blue bands (Bands 1, 2, and 3, respectively, for MODIS, and I1, I2, and M3, respectively, for VIIRS) using their respective spectral response functions (Fig. 2)

$$\rho_b = \sum_{i=1}^{N} w_{b,i}\rho_{G,i} \tag{1}$$

and

$$\sum_{i=1}^{N} w_{b,i} = 1 \tag{2}$$

where ρ_b is the band-averaged reflectance for band b, $\rho_{G,i}$ is the hyperspectral reflectance at the wavelength i, and $w_{b,i}$ is the normalized spectral response for b at i. A-MODIS spectral responses (MODIS Characterization Support Team, 2020) were used to represent both T-MODIS and A-MODIS band reflectances as their bandpass differences were found negligible in a Hyperion-based spectral band compatibility study (Miura and Yoshioka, 2018). For S-VIIRS bands, S-VIIRS Modulated Relative Spectral Responses (RSR) Release 1.0 was adopted. The modulated RSR represent a snapshot of VIIRS spectral performance for 1 February 2013 (orbit 6557) (NOAA STAR Calibration Center, 2017). The S-VIIRS spectral responses were expected to change over time due to the gradual darkening of the VIIRS rotating telescope assembly (RTA) mirror (Cao et al., 2014). By 1 February 2013, approximately 75% of the expected on-orbit mirror darkening had occurred and the remaining 25% darkening was assumed to have occurred at ever-decreasing rates over the following 4 years of the S-VIIRS mission. It should be noted that, whereas MODIS and S-VIIRS red and NIR bandpasses considerably overlap, their blue bandpasses overlap very little (Fig. 2). In addition to the imagery resolution (375 m at nadir) red and NIR bands, S-VIIRS is equipped with moderate-resolution red (M5) and NIR (M7) bands that have the same spatial resolution (750 m at nadir) as the M3 band. In this study, RadCaTS reflectance data were band-averaged to represent I1 and I2 band reflectances because the standard S-VIIRS VI products used I1 and I2 as their input red and NIR reflectances, respectively (Vargas et al., 2013; Didan et al., 2018).

RadCaTS NDVI, EVI, and EVI2 were computed from the MODIS and S-VIIRS bandpass reflectances

$$NDVI = \frac{\rho_{NIR} - \rho_{red}}{\rho_{NIR} + \rho_{red}} \tag{3}$$

$$EVI = G\frac{\rho_{NIR} - \rho_{red}}{\rho_{NIR} + C_1\rho_{red} - C_2\rho_{blue} + L} \tag{4}$$

$$EVI2 = G\frac{\rho_{NIR} - \rho_{red}}{\rho_{NIR} + C\rho_{red} + L} \tag{5}$$

The EVI coefficients of G, C_1, C_2, and L were set to 2.5, 6, 7.5, and 1, respectively, for both the MODIS and VIIRS bandpass reflectances (Huete et al., 2002). The EVI2 coefficients of G, C, and L were set to 2.5, 2.4, and 1, respectively, which were obtained to attain the best compatibility with the EVI for MODIS bandpasses, but used for both the MODIS and VIIRS bandpass reflectances (Jiang et al., 2008).

Made along with the band-averaging and VI computation was the propagation of RadCaTS hyperspectral reflectance uncertainty. Every RadCaTS hyperspectral reflectance was provided with per-band standard uncertainty values. The standard uncertainty of ρ_b, denoted by $u(\rho_b)$, was estimated from the standard uncertainties of $\rho_{G,i}$, denoted by $u(\rho_{G,i})$, by the law of propagation of uncertainty (Taylor and Kuyatt, 2007)

$$u^2(\rho_b) = \sum_{i=1}^{N}\sum_{j=1}^{N} w_{b,i}w_{b,j}u(\rho_{G,i}\rho_{G,j})$$

$$= \sum_{i=1}^{N} w_{b,i}u^2(\rho_{G,i}) + 2\sum_{i=1}^{N-1}\sum_{j=i+1}^{N} w_{b,i}w_{b,j}u(\rho_{G,i})u(\rho_{G,j})r_{i,j} \tag{6}$$

where $r_{i,j}$ is the correlation coefficient between the errors in $\rho_{G,i}$ and $\rho_{G,j}$. The NDVI uncertainty due to the RadCaTS reflectance, u(NDVI), was estimated from $u(\rho_b)$ with the NDVI uncertainty propagation equation (Miura et al., 2000)

$$u^2(NDVI) = \left(\frac{\partial NDVI}{\partial \rho_{NIR}}\right)^2 u^2(\rho_{NIR}) + \left(\frac{\partial NDVI}{\partial \rho_{red}}\right)^2 u^2(\rho_{red}) + 2\frac{\partial NDVI}{\partial \rho_{NIR}}\frac{\partial NDVI}{\partial \rho_{red}}u(\rho_{NIR})u(\rho_{red})r_{NIR,red} \tag{7}$$

and

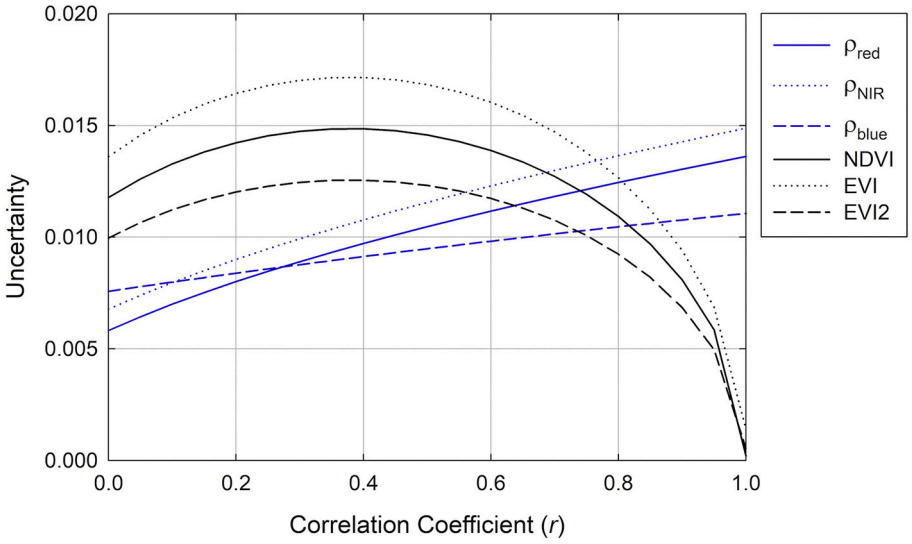

Fig. 3. Changes in the mean uncertainties of the MODIS bandpass reflectances and VIs as a function of band-to-band correlation in the RadCaTS hyperspectral reflectance errors.

$$\frac{\partial NDVI}{\partial \rho_{NIR}} = \frac{2\rho_{red}}{(\rho_{NIR}+\rho_{red})^2} \quad (8)$$

$$\frac{\partial NDVI}{\partial \rho_{red}} = \frac{-2\rho_{NIR}}{(\rho_{NIR}+\rho_{red})^2} \quad (9)$$

The uncertainty propagation equations for the EVI and EVI2 are provided in Appendix I.

In using these uncertainty propagation equations, the band-to-band correlation of 0.75 was assumed for all the band pairs. As described in Section 2, the playa reflectance is known to fluctuate across seasons due primarily to the moisture content of the surface. Thus, the selected spectral reflectance would most likely differ from unmeasured "true" spectral reflectance not in spectral signature, but in overall magnitude (Czapla-Myers et al., 2016), making positively-correlated errors across bands reasonable. To find an appropriate band-to-band correlation value, we computed uncertainties of the band-averaged MODIS reflectances and VIs at 12:00 pm PST for the entire data period (1 April 2013 to 20 September 2019) with the correlation coefficient values between 0 and 1 at 0.05 intervals. The propagated uncertainties linearly increased with increasing correlation values for the band-averaged reflectances (Fig. 3). The VI uncertainties were, however, the highest when the band-to-band correlations were 0.40, lower and about the same when they were 0 and 0.75, and the smallest when they were unity (Fig. 3). Given that the picking of a representative spectrum from the *in situ* hyperspectral reflectance database is one significant source of the RadCaTS surface reflectance uncertainty (Czapla-Myers and Woolliams, 2018), the correlation value of 0.75 was assumed for this study.

3.2. Satellite data

T-MODIS and A-MODIS daily gridded surface reflectance products (MOD09GA and MYD09GA Collection 6, respectively) (Vermote and Wolfe, 2015a; Vermote and Wolfe, 2015b) were obtained for the same period of 1 April 2013 to 20 September 2019 from the NASA EarthData (https://earthdata.nasa.gov/). Four 500-m pixels located over the RadCaTS 1 km-by-1 km area were extracted from the daily gridded products. The extracted pixels (4 pixels per day for each of T-MODIS and A-MODIS) were subjected to per-pixel quality assessment (QA)-flag screening, and retained only when all the four pixels passed the QA-flag screening. Six per-pixel QA flags were used for the screening: land, confidently clear, no adjacent cloud, no snow, no MOD09/MYD09-internal cloud, and no MOD09/MYD09-internal snow. Other QA-flags were also examined but, due mainly to the aerosol quantity flag which misclassified the bright playa surface as a hazy atmosphere (Bruegge et al., 2019), resulted in apparent overscreening of pixel observations, and left a small number of observations in the derived time series data upon the screening. The NDVI, EVI, and EVI2 (Eqs. 3, 4, and 5, respectively) were computed after the screening. They were reduced into daily mean and standard deviation values along with the input red, NIR, and blue reflectances, and view zenith and azimuth, and sun zenith and azimuth angles. The RadCaTS site is a well-characterized, 1 km-by-1 km area located in the middle of a much larger, spatially extensive and pseudo-homogeneous playa surface (Fig. 1). This very nature of the site should have served to minimize or to reduce the impacts of pixel mis-registration and deformation onto the analysis. We estimated, using the mis-registration and footprint dimension parameters found in Wolfe et al. (1998, 2002), that MODIS pixel observations with a range of footprint sizes and mis-registration were always located within the playa surface whereas their coverage could extend beyond the 1 km-by-1 km RadCaTS area.

S-VIIRS VI, surface reflectance, and geo-angle swath/granule products (VIVIO, IVISR, and GITCO, respectively) (Vargas et al., 2013; Vermote et al., 2014; Wolfe et al., 2013) were obtained for a period from 1 April 2013 to 31 August 2019 from the NOAA Comprehensive Large Array-data Stewardship System (https://www.class.noaa.gov). The NDVI and EVI contained in the VI products, red (I1), NIR (I2), and blue (M3) reflectances contained in the surface reflectance products, and view zenith and azimuth, and sun zenith and azimuth angles contained in the geo-angle products were remapped, by nearest neighbor resampling, onto a 0.00375-degree linear latitude-longitude grid for a 70 km-by-70 km region having the RadCaTS 1 km-by-1 km area at the center. Before the remapping, VIIRS moderate-resolution layers, including blue (M3) reflectance, view zenith and azimuth, and sun zenith and azimuth angles, were spatially pseudo-enhanced into the imagery resolution by repeating one moderate-resolution pixel four times (2-by-2) to retain the original imagery-to-moderate resolution band integrity. The remapping was performed on a per-orbit basis as VIIRS ground swaths from two adjacent orbits overlapped significantly (~30%). After the remapping, the EVI2 was computed from the red and NIR reflectances (Eq. 5), and the EVI was multiplied by 1.25 to adjust the gain as the gain factor of 2.0 was adopted in the VIIRS VI algorithm (Vargas et al., 2013). Every VIIRS subset scene was then visually inspected for cloud or shadow contaminations using true- and false-colour composites, and labeled as

confidently clear, probably clear, probably cloudy/shadowy, or confidently cloudy/shadowy. VI, reflectance, and geo-angle data were extracted over a 3 pixels-by-3 pixels window corresponding to the RacCaTS 1 km-by-1 km area from every VIIRS scene labeled as confidently clear or probably clear, and reduced into means and standard deviations.

Three additional data screening procedures were applied to the derived T-MODIS, A-MODIS, and S-VIIRS time series data. First, apparent outliers whose reflectances or VIs were either extremely higher or lower than all other points were identified. For every apparent outlier, true- and false-colour composites and daily weather data (described in Section 3.3 below) of the corresponding dates were examined. We removed them when the corresponding true- and false-colour composites indicated the presence of clouds or cloud shadows, or when it rained on the corresponding dates. Second, those observations with negative EVI values were considered invalid and removed from the dataset. Visual inspections of true- and false-colour composites of all these negative EVIs indicated that they were associated with cloud shadows. Finally, we removed those reflectances or VIs with large standard deviations. Visual inspection of the corresponding true- and false-colour composites indicated that they were associated with clouds and cloud shadows, or pixels coming from two different orbits for T-MODIS and A-MODIS data.

The VIIRS atmospheric correction algorithm is a heritage of the MODIS atmospheric correction algorithm (Vermote et al., 2014). Their main algorithmic differences, as implemented in generating the MODIS and VIIRS surface reflectance products used in this study, were in their atmospheric water vapor data sources and aerosol retrieval algorithms. Whereas the MODIS algorithm used MODIS precipitable water vapor products, the National Center for Environmental Prediction (NCEP) precipitable water vapor products were used in the VIIRS atmospheric correction (Jackson et al., 2013; Vermote and Kotchenova, 2008). Both MODIS and VIIRS aerosol retrievals were made with a modified version of the dark target (DT) approach (Kaufman et al., 1997). In brief, this approach retrieved aerosol optical thickness based on an empirically-derived, expected relationship between the blue and red surface reflectances (Vermote and Kotchenova, 2008; Jackson et al., 2013). In the VIIRS algorithm, the globally-constant blue-to-red band ratio of 0.645 was used (Jackson et al., 2013). In the MODIS algorithm, the band ratio was defined as a function of the surface brightness, but apparently around 0.5 (Vermote and Saleous, 2006).

3.3. Weather data

Daily weather data (precipitation, snowfall, and maximum and minimum temperatures) at the Blue Eagle Ranch weather station (N 38.5208° and W 115.5444° at 1425.9 m above MSL) (Fig. 1) were obtained from the Global Historical Climatology Network of the NOAA National Center for Environmental Information (https://www.ncdc.noaa.gov/data-access/land-based-station-data/land-based-datasets/global-historical-climatology-network-ghcn). The data record at the station covered a period from 1 April 1978 to 1 April 2019 and, thus, we obtained data from 1 January 2013 to 31 March 2019. This daily data record was reduced into monthly time series data. Daily precipitation and snowfalls were summed over every month, and daily maximum and minimum temperatures were averaged over every month period to obtain monthly values.

3.4. Data analysis

We first compared MODIS and VIIRS nadir VIs and reflectances (view zenith angle, θ_v, $< 1.8°$ for both T-MODIS and S-VIIRS) to the RadCaTS counterparts. As there were no nadir observations with A-MODIS over the site, we selected those observations of which view zenith angles were closest to nadir ($\theta_v = 4$–$5.6°$ in the backward scattering direction with respect to the Sun position, and $\theta_v = 6$–$7.7°$ in the forward scattering direction with respect to the Sun position). RadCaTS data acquired at 10:30 am PST, 1:00 pm PST, and 12:30 pm PST were used to compare with T-MODIS, A-MODIS, and S-VIIRS data, respectively, based on the solar positions.

Table 1
View zenith angle bins designated for satellite data subsets.

Satellite Sensor	T-MODIS	A-MODIS	S-VIIRS
Number of Bins	9 for each of forward and backward scattering directions	9 for each of forward and backward scattering directions	11 for each of forward and backward scattering directions
View Zenith Angle Bins	0.0°-1.8° 10.0°-13.3° 21.1°-24.2° 30.7°-33.6° 39.1° – 41.8° 46.1°-48.6° 52.0°-54.3° 56.9°-59.0° 61.1°<	3.9°-7.7° 15.6° – 19.0° 26.0°-29.0° 35.4°-37.6° 43.2° – 44.9° 49.9°-51.0° 55.3°-56.1° 59.7°-60.4° 62.9°<	0.0° – 1.8° 8.9°-11.9° 18.9°-21.5° 27.9°-30.3° 36.1°-37.9° 43.0°-44.5° 48.7°-50.3° 53.7°-55.3° 57.9°-59.7° 61.6° – 63.4° 64.9°<

The number of coincident satellite-RadCaTS observations were typically 10 per year for T-MODIS, A-MODIS, and S-VIIRS, as RadCaTS data were not always available when satellite data were available. In order to utilize all the available data for the satellite-RadCaTS comparison, we employed multiple linear regression with dummy variables

$$y = \beta_0 + \beta_1 t + \beta_2 S + \beta_3 t \cdot S + \varepsilon \quad (10)$$

where y is the reflectance or VI, t is the observation date of y, S is the dummy variable where $S = 1$ for y being a satellite observation and $S = 0$ for y being an *in situ* RadCaTS observation, β_i ($i = 0, 1, \ldots, 3$) are the regression coefficients, and ε is the unexplained error term. When β_2 is significant, the satellite and ground observations are subject to a systematic difference. When β_3 is significant, the satellite temporal trend had a different slope from that of the ground measurements. The model was fit in a step-wise manner, *i.e.*, first only with β_0 and β_1, then with β_0, β_1 andβ_2, and finally as a full model with all the four parameters (β_0 - β_3) to estimate.

As the above regression analysis assumed linear trends, the non-parametric Mann-Kendall (MK) monotonic trend test was also performed to examine whether each reflectance or VI temporal dataset had an increasing or decreasing trend (Kendall, 1975; Hipel and McLeod, 1994; Libiseller and Grimvall, 2002). The MK test has been utilized for identifying temporal and spatial trends in the NDVI and fractional vegetation cover (Bhimala et al., 2020; Wu et al., 2014). Kendall's τ was used to evaluate the direction of the monotonic trend (*i.e.*, decreasing or increasing). The MK tests were performed using R 4.0.2 (R Core Team, 2020) and the trend (v1.1.4; Pohlert, 2020) package in this study.

We then investigated the behavior of off-nadir VIs for each of T-MODIS, A-MODIS, and S-VIIRS. Each of the T-MODIS, A-MODIS, and S-VIIRS datasets was divided into subsets based on view zenith angles. For each satellite, a limited number of distinctive view zenith angles occurred for the RadCaTS site. View zenith angle bins were designated to correspond to these view zenith angle ranges (Table 1).

Two analyses were performed on the subsets. First, we plotted the view zenith angle against the red, NIR, and blue reflectances for each satellite to examine the changes in the reflectance and variations as a function of view zenith angle. Second, the soil line equation was fit to NIR-red reflectance pairs for every subset (view zenith angle bin) and we examined variations in the fitted soil lines across the view zenith angle bins (*e.g.*, Yoshioka et al., 2010)

$$R_{sN} = aR_{sR} + b \quad (11)$$

where a and b are the soil line parameters, and R_{sN} and R_{sR} are the

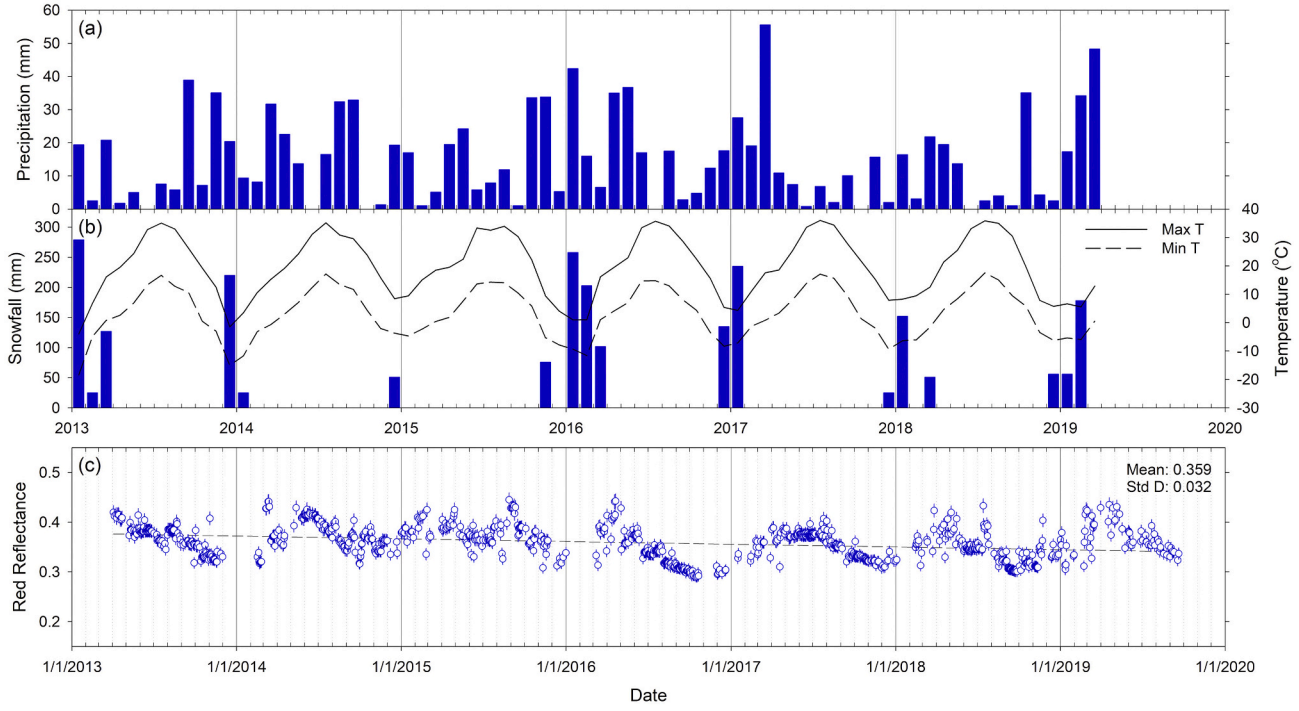

Fig. 4. Comparison of weather data at the Blue Eagle Ranch weather station and playa surface reflectance measured by the RadCaTS facility. (a) Monthly precipitation, (b) monthly snowfall, and maximum and minimum monthly temperatures, and (c) RadCaTS surface reflectance band-averaged for MODIS red bandpass acquired at 12:00 pm PST. (For interpretation of the references to colour in this figure legend, the reader is referred to the web version of this article.)

NIR and red reflectances of the playa, respectively. We applied the same analysis to the red-blue reflectance relationship where the red reflectance was regressed against the blue reflectance. Since the primary source of variability in the playa surface reflectance was the moisture content (see Section 2), we expected the red and NIR, and red and blue reflectances each to form a soil line in their respective cross-reflectance spaces for every view zenith angle bin. With respect to view zenith angles, we expected that soil lines would be slightly different across view zenith angle bins. Wang et al. (2014) reported their laboratory experiment results in which soil reflectance was higher in the backward scattering direction than in the forward scattering direction, but exhibited a greater range of values in the NIR than at the visible wavelengths (*i.e.*, wavelength-dependent).

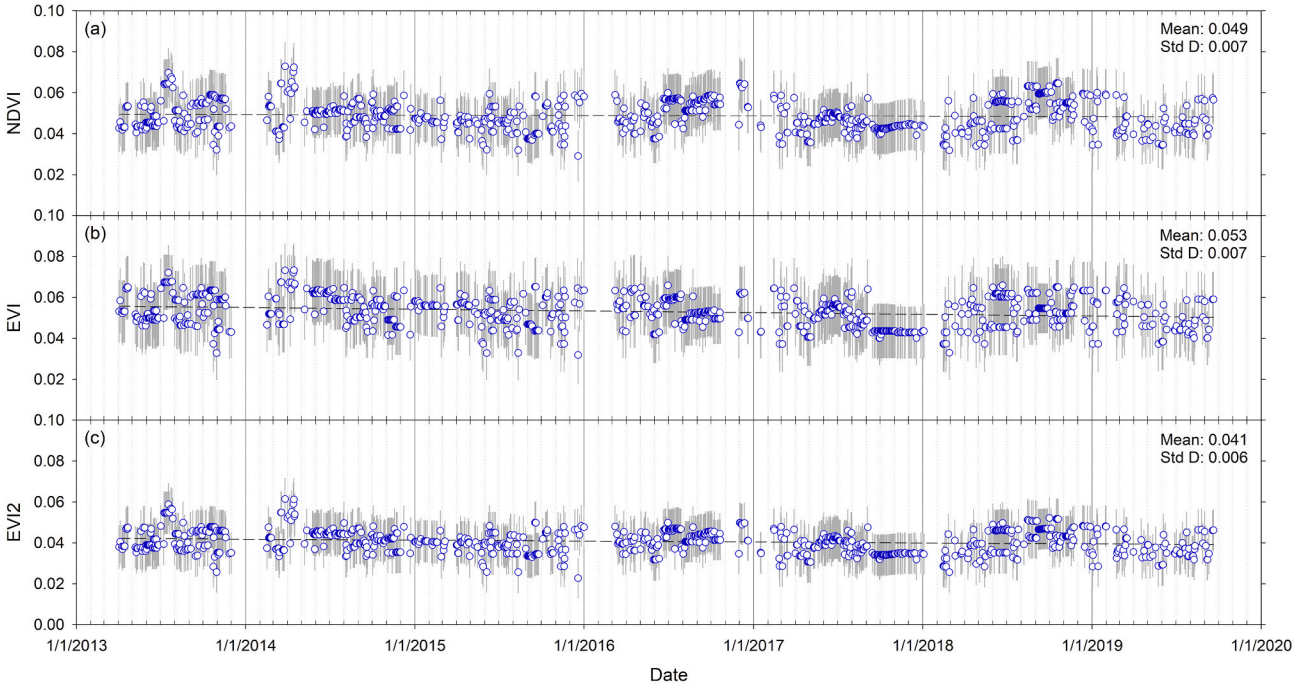

Fig. 5. VIs derived from RadCaTS-measured surface reflectances (MODIS bandpasses, 12:00 pm PST): (a) NDVI, (b) EVI, and (c) EVI2. The gray vertical bars are the standard uncertainty.

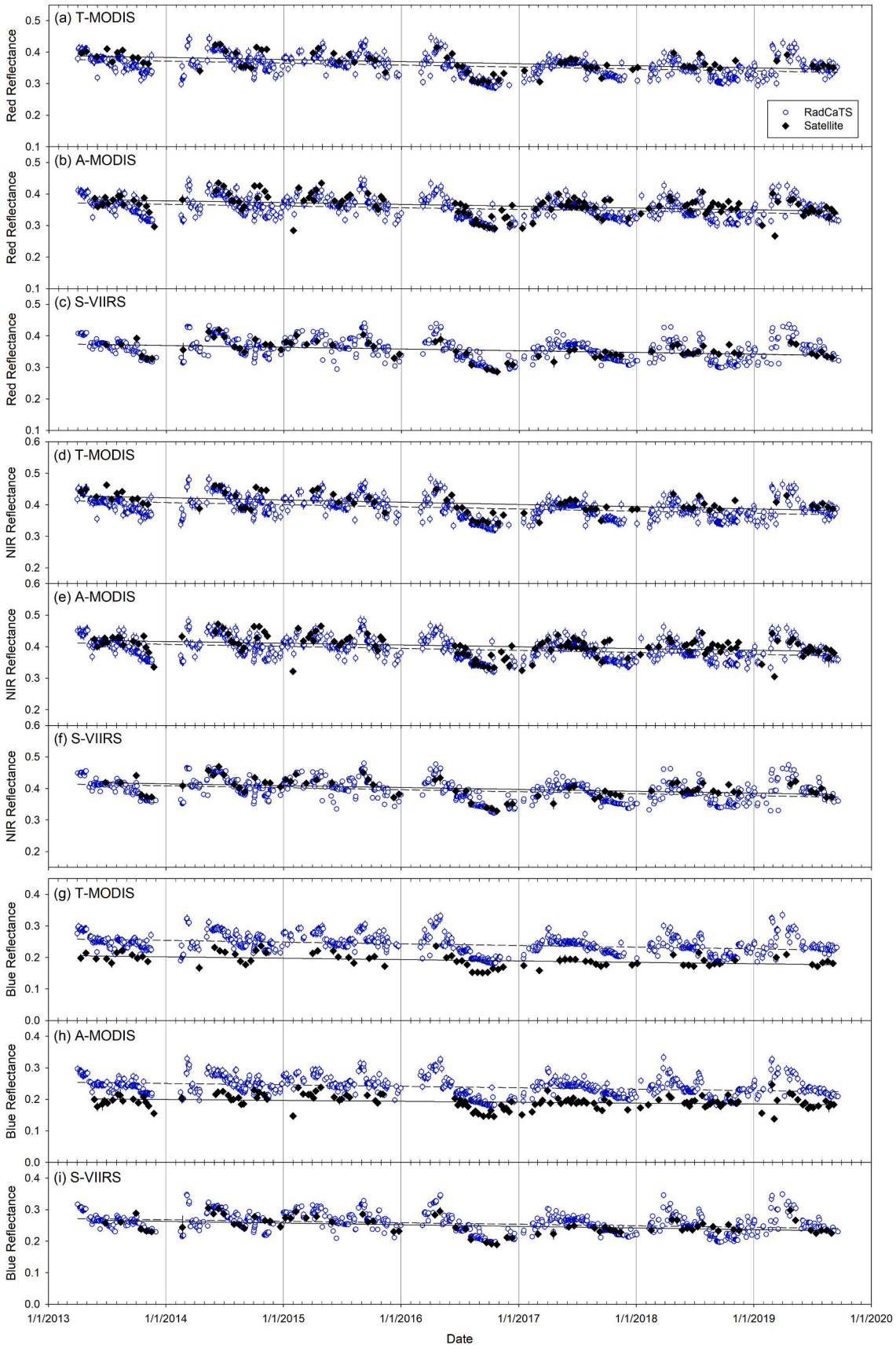

Fig. 6. Comparison of satellite-measured surface reflectances to RadCaTS (ground-measured) counterparts over the RadCaTS site: (a) T-MODIS red, (b) A-MODIS red, (c) S-VIIRS red, (d) T-MODIS NIR, (e) A-MODIS NIR, (f) S-VIIRS NIR, (g) T-MODIS blue, (h) A-MODIS blue, and (i) S-VIIRS blue reflectances. (For interpretation of the references to colour in this figure legend, the reader is referred to the web version of this article.)

Table 2
Summary statistics of satellite (near-nadir observations only) and RadCaTS reflectances over the RadCaTS site. The numbers in parentheses are standard deviations.

Sensor	Red Reflectance		NIR Reflectance		Blue Reflectance	
	Satellite	RadCaTS	Satellite	RadCaTS	Satellite	RadCaTS
T-MODIS	0.367 (0.030)	0.356 (0.032)	0.405 (0.031)	0.391 (0.033)	0.191 (0.020)	0.241 (0.029)
A-MODIS	0.363 (0.033)	0.354 (0.031)	0.401 (0.032)	0.392 (0.033)	0.192 (0.021)	0.240 (0.029)
S-VIIRS	0.355 (0.028)	0.356 (0.032)	0.399 (0.030)	0.394 (0.033)	0.249 (0.026)	0.257 (0.030)

Table 3
Results of regression analysis with dummy variables for satellite (near-nadir observations only) and RadCaTS reflectances. The numbers in parentheses are standard errors.

Band	Sensor	Parameter Estimate[a] (Standard Error)			
		b_0	b_1	b_2	b_3
Red	T-	6.49e-01	-1.73e-05	1.10e-02	n.
	MODIS	(2.21e-02) ***	(1.30e-06) ***	(3.54e-03) **	s.
	A-	6.07e-01	-1.49e-05	1.03e-02	n.
	MODIS	(2.28e-02) ***	(1.34e-06) ***	(2.81e-03) ***	s.
	S-VIIRS	6.14e-01	-1.52e-05	8.50e-05	n.
		(2.35e-02) ***	(1.38e-06) ***	(3.74e-03) n.s.	s.
NIR	T-	7.07e-01	-1.87e-05	1.45e-02	n.
	MODIS	(2.29e-02) ***	(1.35e-06) ***	(3.66e-03) ***	s.
	A-	6.86e-01	-1.73e-05	1.14e-02	n.
	MODIS	(2.32e-02) ***	(1.37e-06) ***	(2.86e-03) ***	s.
	S-VIIRS	6.86e-01	-1.72e-05	7.38e-03	n.
		(2.37e-02) ***	(1.40e-06) ***	(3.78e-03) .	s.
Blue	T-	4.86e-01	-1.44e-05	-4.99e-02	n.
	MODIS	(2.05e-02) ***	(1.21e-06) ***	(3.28e-03) ***	s.
	A-	4.43e-01	-1.20e-05	-4.62e-02	n.
	MODIS	(2.06e-02) ***	(1.22e-06) ***	(2.55e-03) ***	s.
	S-VIIRS	4.79e-01	-1.32e-05	-6.35e-03	n.
		(2.26e-02) ***	(1.33e-06) ***	(3.60e-03) .	s.

[a] - '***' – significant at <0.001; '**' – significant at 0.01; '*' – significant at 0.05; '.' – significant at 0.10; 'n.s.' – not significant (p-value >0.10).

4. Results

4.1. Weather and RadCaTS data

Monthly precipitation varied largely throughout the study period, with weak seasonality of higher winter rainfall (Fig. 4a). Snowfalls also varied from year to year, but only occurred from November to March (Fig. 4b). The highest monthly maximum and minimum temperatures occurred in July every year, except for the year 2015, and the former was about the same throughout the study period (Fig. 4b). The maximum and minimum temperatures of the winter months varied from year to year and were lower for the winters with a higher snowfall amount (*i.e.*, 2013, 2014, and 2016).

Plotted in Fig. 4c are RadCaTS red reflectance values, band-averaged for the MODIS bandpass. The red reflectance ranged from 0.3 to 0.45, varying throughout the study period. The reflectance was generally higher in April to May and lower in October to December, but did not change seasonally in a predictable cyclic manner and varied from year to year. Overall, the red reflectance decreased during the study period according to the simple linear regression analysis and MK test results [slope = −1.50e-5 per day (p-value <0.001) and $\tau = -0.242$ (p-value <0.001), respectively]. RadCaTS NIR and blue reflectances temporally varied in parallel to the red reflectance (not shown here). Their means and standard deviations were 0.396 ± 0.033 (NIR) and 0.243 ± 0.030 (blue), and both reflectances had decreasing trends [slope = −1.70e-5 per day (p-value <0.001) and $\tau = -0.262$ (p-value <0.001) for the NIR; and slope = −1.16e-5 per day (p-value <0.001) and $\tau = -0.207$ (p-value <0.001) for the blue].

The NDVI, EVI, and EVI2 computed from those RadCaTS reflectances were very low, and all had reasonably flat temporal signatures while being subject to short-term variations (Fig. 5). The NDVI had a very weak decreasing trend, but it was not statistically significant [slope = −5.10e-7 per day (p-value = 0.13) and $\tau = -0.032$ (p-value = 0.14)], whereas the EVI and EVI2 had decreasing trends (slope = −2.28e-6 per day and − 1.25e-6 per day, respectively, and $\tau = -0.145$ and − 0.089, respectively, and p-value <0.001 for all).

4.2. Satellite and RadCaTS comparison of reflectances

The red, NIR, and blue reflectances of all the three sensors increased and decreased at the same time as their *in situ* counterparts, following the comparable seasonal and inter-annual changes throughout the study period (Fig. 6). Both the means and regression analysis results indicated that T-MODIS and A-MODIS red reflectances were higher than their RadCaTS counterparts by ~0.01 (Tables 2 and 3). T-MODIS and A-MODIS NIR reflectances were also higher than their *in situ* counterparts by more than 0.01. VIIRS red reflectance was not different from the *in situ* counterpart, whereas VIIRS NIR reflectance was slightly higher than the *in situ* counterpart. T-MODIS and A-MODIS blue reflectances were consistently lower than the RadCaTS counterparts by ~0.05. S-VIIRS blue reflectance was also lower than the RadCaTS counterpart by ~0.007. The regression analysis results indicated that all these satellite reflectances had the same decreasing trends as their respective *in situ* counterparts (b_1 being negative values and b_3 not significant; see Table 3). The MK test results also indicated that all the satellite and *in situ* reflectances had decreasing trends (negative τ values; see Table 4).

4.3. Satellite and RadCaTS comparison of VIs

The NDVI of all the three satellite sensors increased and decreased at the same time as their *in situ* counterparts (Fig. 7a-c). The satellite NDVIs noticeably increased during the last half of the year 2016, which corresponded to a period of low reflectances (see Fig. 6). T-MODIS NDVI was only slightly higher than the RadCaTS (by 0.003 NDVI units) (Table 5 and b_2 in Table 6). A-MODIS NDVI appeared slightly lower than the RadCaTS counterpart for 2013–2015, but were comparable with RadCaTS for the reminder of the period. S-VIIRS NDVI were consistently higher than the RadCaTS counterpart.

Table 4
Mann-Kendall test results (τ values[a]) for satellite (near-nadir observations only) and RadCaTS reflectances.

Sensor	Red Reflectance		NIR Reflectance		Blue Reflectance	
	Satellite	RadCaTS	Satellite	RadCaTS	Satellite	RadCaTS
T-MODIS	−0.294 ***	−0.275 ***	−0.286 ***	−0.280 ***	−0.280 ***	−0.269 ***
A-MODIS	−0.304 ***	−0.241 ***	−0.273 ***	−0.267 ***	−0.259 ***	−0.230 ***
S-VIIRS	−0.175 *	−0.243 ***	−0.187 *	−0.264 ***	−0.164 *	−0.220 ***

[a] - '***' – significant at <0.001; '**' – significant at 0.01; '*' – significant at 0.05; '.' – significant at 0.10; 'n.s.' – not significant (p-value >0.10).

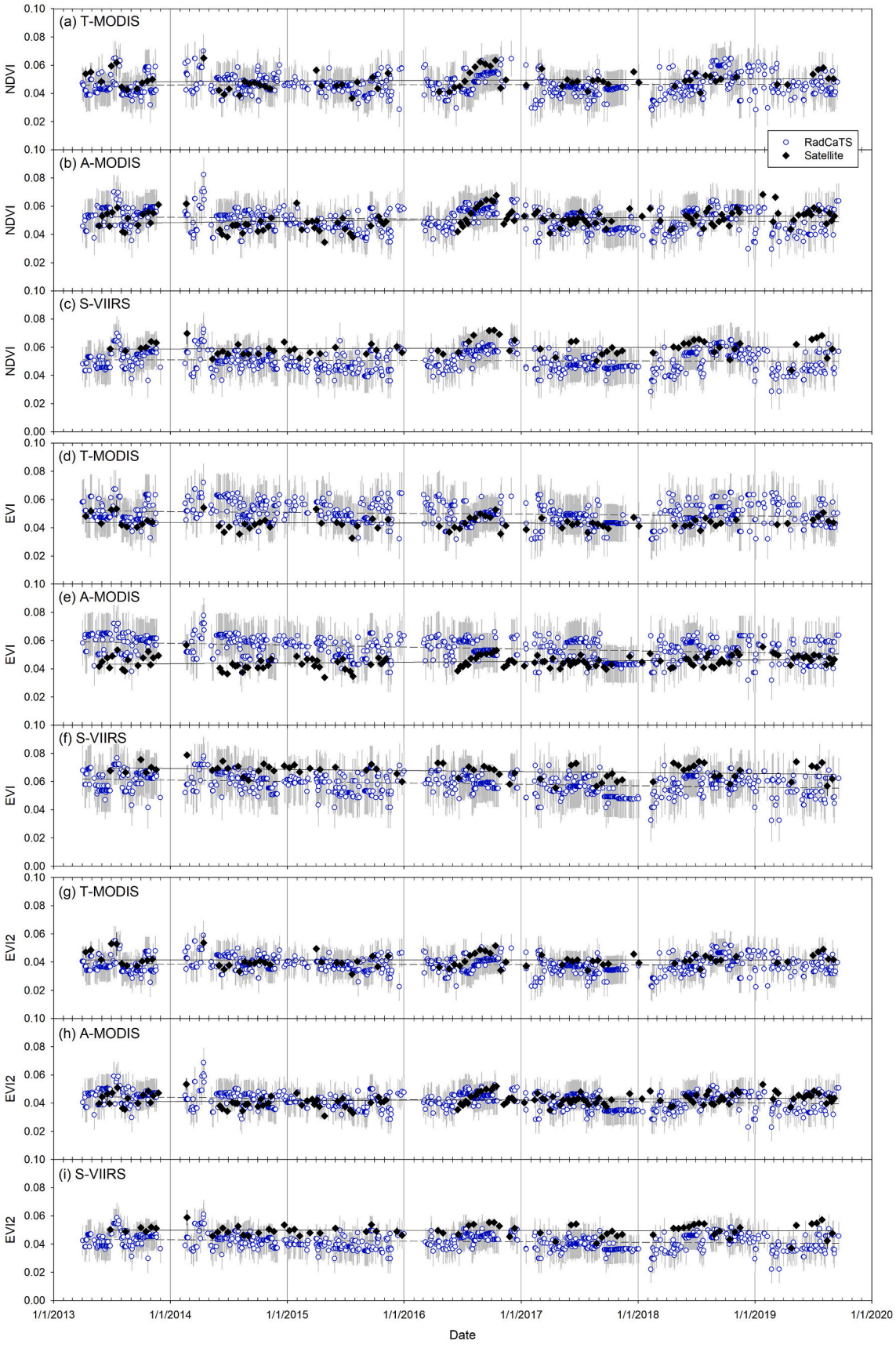

Fig. 7. Comparison of satellite-derived VIs to RadCaTS (ground-measured) counterparts over the RadCaTS site: (a) T-MODIS NDVI, (b) A-MODIS NDVI, (c) S-VIIRS NDVI, (d) T-MODIS EVI, (e) A-MODIS EVI, (f) S-VIIRS EVI, (g) T-MODIS EVI2, (h) A-MODIS EVI2, and (i) S-VIIRS EVI2.

Table 5
Summary statistics of satellite (near-nadir observations only) and RadCaTS VIs over the RadCaTS site. The numbers in parentheses are standard deviations.

Sensor	NDVI		EVI		EVI2	
	Satellite	RadCaTS	Satellite	RadCaTS	Satellite	RadCaTS
T-MODIS	0.049 (0.006)	0.046 (0.007)	0.044 (0.004)	0.050 (0.007)	0.041 (0.005)	0.038 (0.005)
A-MODIS	0.051 (0.006)	0.051 (0.007)	0.045 (0.004)	0.055 (0.008)	0.042 (0.004)	0.042 (0.006)
S-VIIRS	0.059 (0.005)	0.050 (0.007)	0.067 (0.005)	0.059 (0.007)	0.050 (0.004)	0.042 (0.005)

Table 6
Results of regression analysis with dummy variables for satellite (near-nadir observations only) and RadCaTS VIs. The numbers in parentheses are standard errors.

VI	Sensor	Parameter Estimate[a] (Standard Error)			
		b_0	b_1	b_2	b_3
NDVI	T-MODIS	3.85e-02 (5.26e-03) ***	4.47e-07 (3.10e-07) n.s.	3.14e-03 (8.42e-04) ***	n.s.
	A-MODIS	7.68e-02 (5.82e-03) ***	−1.54e-06 (3.43e-07) ***	−6.73e-02 (1.68e-02) ***	3.96e-06 (9.85e-07) ***
	S-VIIRS	5.66e-02 (5.34e-03) ***	−3.66e-07 (3.15e-07) n.s.	9.06e-03 (8.52e-04) ***	n.s.
EVI	T-MODIS	7.72e-02 (5.40e-03) ***	−1.61e-06 (3.18e-07) ***	−6.39e-03 (8.64e-04) ***	n.s.
	A-MODIS	1.17e-01 (5.54e-03) ***	−3.68e-06 (3.27e-07) ***	−9.69e-02 (1.60e-02) ***	5.13e-06 (9.38e-07) ***
	S-VIIRS	1.05e-01 (5.12e-03) ***	−2.71e-06 (3.02e-07) ***	9.10e-03 (8.07e-04) ***	n.s.
EVI2	T-MODIS	4.62e-02 (4.09e-03) ***	−4.73e-07 (2.41e-07) .	3.23e-03 (6.54e-04) ***	n.s.
	A-MODIS	7.81e-02 (4.44e-03) ***	−2.11e-06 (2.62e-07) ***	−5.84e-02 (1.28e-02) ***	3.46e-06 (7.52e-07) ***
	S-VIIRS	6.14e-02 (3.94e-03) ***	−1.15e-06 (2.33e-07) ***	7.90e-03 (6.29e-04) ***	n.s.

[a] - '***' – significant at <0.001; '**' – significant at 0.01; '*' – significant at 0.05; '.' – significant at 0.10; 'n.s.' – not significant (p-value >0.10).

For all of T-MODIS, A-MODIS, and S-VIIRS, the EVI was less variable than the NDVI throughout the study period (Fig. 7d-f). Both the means and regression analysis results indicated that T-MODIS EVI and A-MODIS EVI were lower than the RadCaTS counterparts, whereas S-VIIRS EVI was higher than the RadCaTS counterpart (Table 5 and b_2 in Table 6). The EVI2 of all the three satellites had flat temporal signatures comparable to their respective RadCaTS counterparts (Fig. 7g-i). T-MODIS EVI2 and VIIRS EVI2 were higher than the RadCaTS counterparts (Table 5; and b_2 in Table 6).

Both the regression analysis and MK test results indicated that T-MODIS and S-VIIRS NDVIs had neither increasing nor decreasing trends that were the same as their respective RadCaTS counterparts (non-significant b_1 and b_3 in Table 6; and significant τ at 0.10 for T-MODIS NDVI and non-significant τ for all the others in Table 7). For T-MODIS EVI and S-VIIRS EVI, the regression analysis results indicated decreasing trends for both the satellite and *in situ* data (significant b_1 and non-significant b_3 in Table 6), whereas the MK test results indicated decreasing trends for the *in situ* EVIs, but not for the satellite EVIs (Table 7). The regression analysis found weakly decreasing trends for the satellite and *in situ* EVI2 for T-MODIS (significant b_1 at 0.10 and non-significant b_3 in Table 6), but the MK test results indicated no trends for both (Table 7). For S-VIIRS EVI2, the regression analysis and MK test results found a decreasing trend for the *in situ* EVI2, but only the regression analysis found a significant trend for the satellite EVI2 (significant b_1 and non-significant b_3 in Table 6; and significant and non-significant τ for the RadCaTS and satellite, respectively, in Table 7). It was only A-MODIS of which satellite and *in situ* VIs showed different trends. All the three A-MODIS satellite VIs had increasing trends, whereas all the RadCaTS counterparts showed decreasing trends (Tables 6 and 7).

In summary, the satellite VI temporal variations coincided with those of the *in situ* counterparts well. Other key results are summarized below:

- T-MODIS and A-MODIS NDVIs and EVI2s were only slightly different (higher or lower) from the *in situ* counterparts.
- The NDVI, EVI, and EVI2 of S-VIIRS were all consistently higher than the *in situ* counterparts.
- The EVI was most inconsistent among the sensors, which was lower than the *in situ* data for T-MODIS and A-MODIS, but higher for S-VIIRS.
- It was only A-MODIS VIs that had increasing trends for the study period.

4.4. Analysis of off-nadir reflectances and VIs

Plotted in Fig. 8. are T-MODIS off-nadir reflectances and VIs as an example. The red, NIR, and blue reflectances of the backward and forward scattering geometries show similar temporal variations, but the former was much higher than the latter (Fig. 8a-c). The NDVI was higher in the forward scattering direction than in the backward scattering direction (Fig. 8d). The EVI and EVI2 were also higher for the forward scattering geometry than for the backward scattering geometry, but their differences were smaller than those observed for the NDVI (Fig. 7e, f).

In Fig. 9, view zenith angles are plotted against red reflectances in order to assess the change in red reflectance as a function of view zenith angle. The red reflectance varied the smallest at nadir or near-nadir view zenith angles, their values ranging for 0.30–0.43, 0.27–0.44, and 0.29–0.43 for T-MODIS, A-MODIS, and S-VIIRS, respectively. With increasing view zenith angles, the red reflectances under the forward scattering geometry decreased and those under the backward scattering geometry increased, overall variations in reflectance increasing for all

Table 7
Mann-Kendall test results (τ values[a]) for satellite (near-nadir observations only) and RadCaTS VIs.

Sensor	NDVI		EVI		EVI2	
	Satellite	RadCaTS	Satellite	RadCaTS	Satellite	RadCaTS
T-MODIS	0.148 .	0.028 n.s.	0.028 n.s.	−0.103 ***	0.090 n.s.	−0.034 n.s.
A-MODIS	0.356 ***	−0.085 ***	0.360 ***	−0.243 ***	0.334 ***	−0.151 ***
S-VIIRS	0.045 n.s.	−0.023 n.s.	−0.116 n.s.	−0.185 ***	−0.019 n.s.	−0.094 ***

[a] - '***' – significant at <0.001; '**' – significant at 0.01; '*' – significant at 0.05; '.' – significant at 0.10; 'n.s.' – not significant (p-value >0.10).

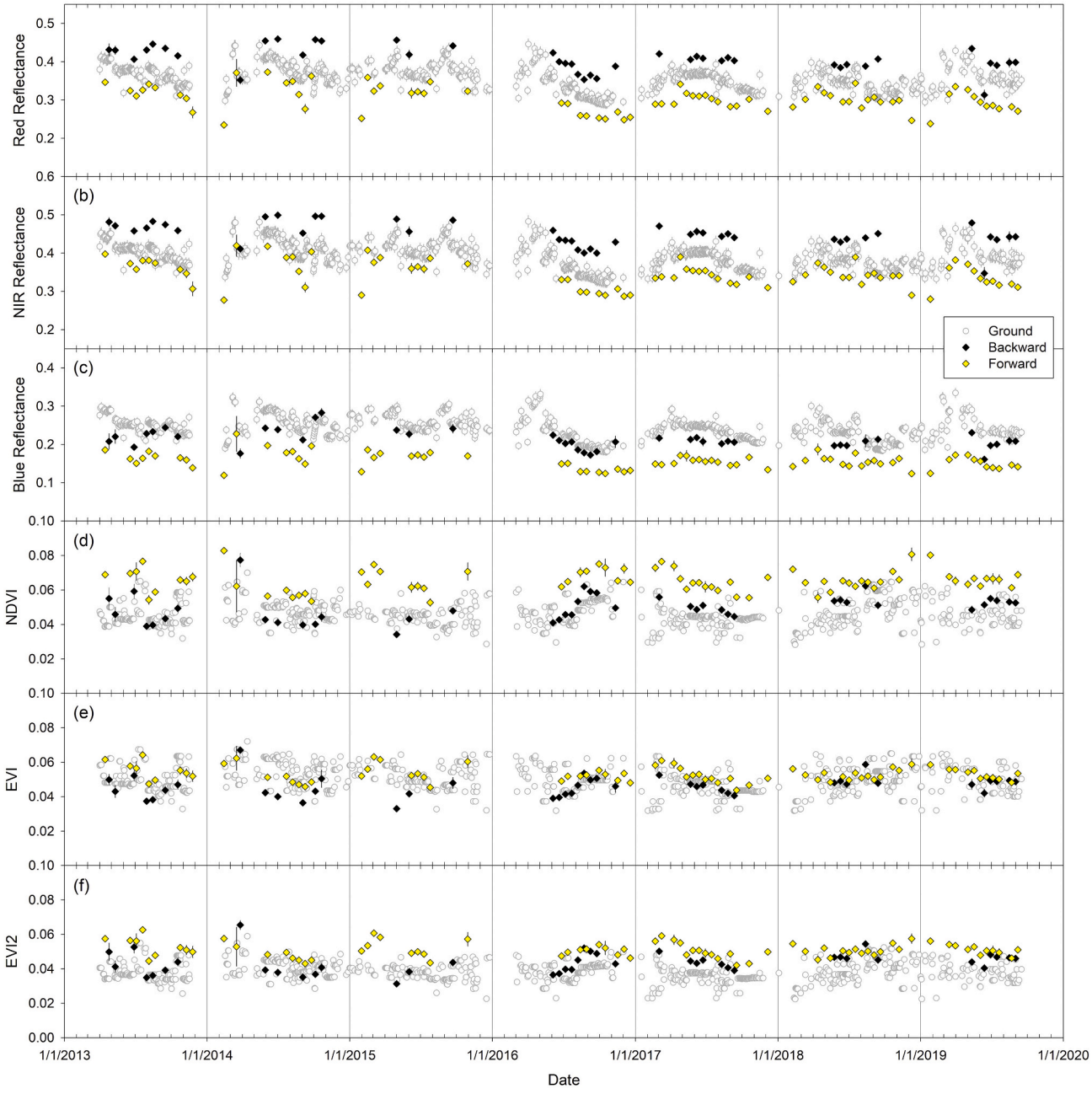

Fig. 8. Temporal profiles of T-MODIS off-nadir reflectances and VIs over the RadCaTS site. View zenith angles were ~ 48° and ~ 47° for backward and forward scattering geometries, respectively.

the three sensors (Fig. 9). The same view zenith angle-reflectance relationships were observed for the NIR and blue reflectances (not shown).

The red and NIR reflectances formed linear relationships for each of the three sensors as expected (Fig. 10a-c). For T-MODIS, most of those regression lines (soil lines) derived for each view zenith angle bin overlapped and were not very different from a global regression line (soil line) which was derived from all the data (Fig. 10a). These soil lines were nearly parallel to the 1:1 line. The derived regression/soil lines for A-MODIS and S-VIIRS had the same behavior (Fig. 10b and c, respectively). In Fig. 10d and e, the corresponding RadCaTS reflectances are plotted for comparison, although they were limited to nadir reflectances. These plots indicated that the red-NIR soil lines derived from the satellite data were basically comparable to those derived with RadCaTS reflectances. These results also support that the lower and higher reflectances due to larger view zenith angles plot along the same soil line (wider variations along the same soil line).

In Fig. 11, we repeat the same analysis for the red and blue reflectances. The red and blue reflectances also formed robust soil lines for all of the satellite sensor data (Fig. 11a-c). Soil lines derived for each view zenith angle bin had wider variations than those for the red-NIR soil lines, but these lines resided within the 95% prediction intervals of the global soil lines reasonably well. These robust relationships indicated that the off-nadir reflectances could be treated as the wider variations along the same soil line in the red-blue reflectance space as well.

Unlike the red-NIR relationships, however, the red-blue relationships were slightly different between MODIS and VIIRS, and between the satellites and RadCaTS (Fig. 11). The RadCaTS relationships were nearly parallel to the 1:1 line, whereas the soil lines derived for the satellite data had higher slopes, corresponding to the previous analysis results

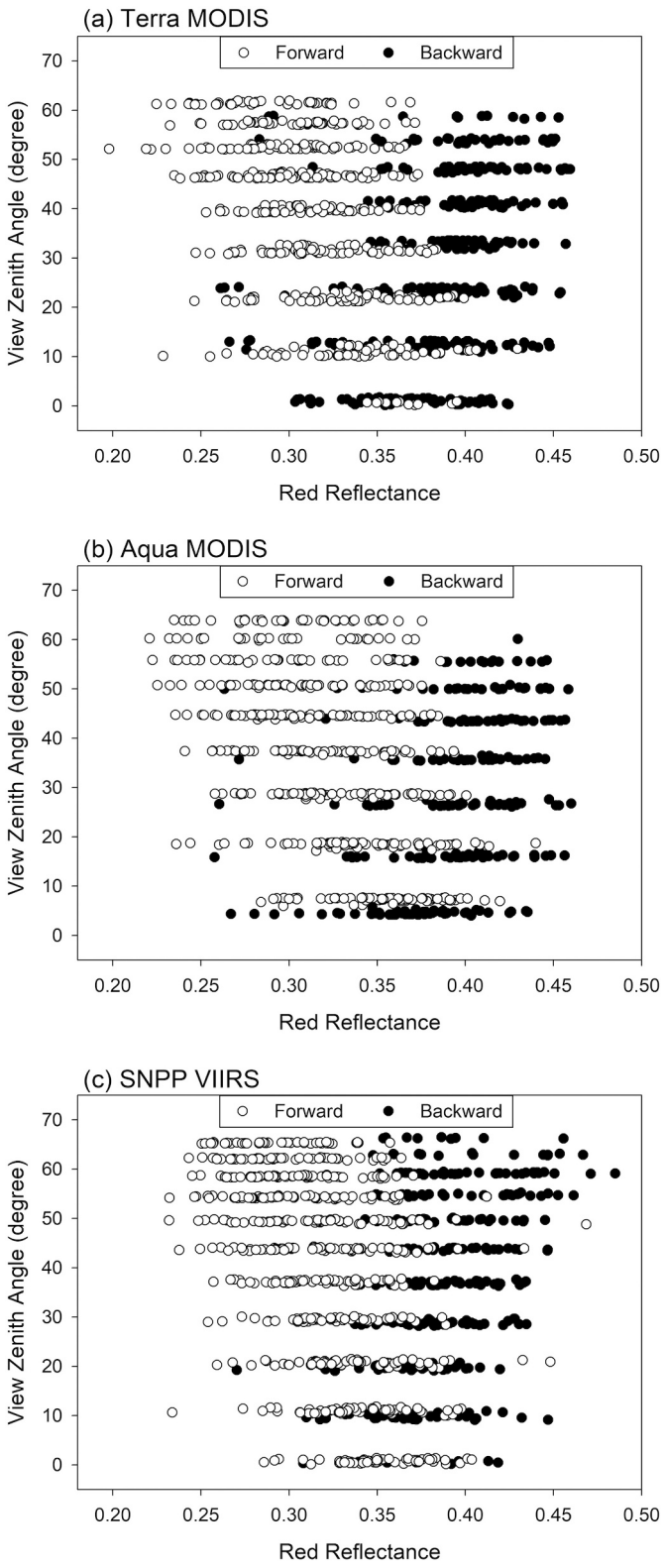

Fig. 9. View zenith angle *vs.* red reflectance plots for (a) T-MODIS, (b) A-MODIS, and (c) S-VIIRS. (For interpretation of the references to colour in this figure legend, the reader is referred to the web version of this article.)

where the satellite-measured blue reflectances were lower than the RadCaTS counterparts (Fig. 6).

As the reflectance changes due to both the surface and viewing geometry conditions could be explained by the variations along the same soil lines, the derived empirical soil lines and their 95% prediction intervals were projected onto the greenness (represented by VIs)-brightness (represented by the red reflectance) space (Fig. 12). The transformed soil lines were used to assess the satellite VI behaviors as a function of the soil brightness variations, *i.e.*, how the soil lines aligned with the VI isolines (the gridlines parallel to the *x*-axis in each plot in Fig. 12) for each of the three VIs, and how the soil lines compared with those depicted by the *in situ* RadCaTS data. The NDVI decreased with increasing red reflectances for all the three sensors (Fig. 12a, d, g). The 95% prediction intervals indicated that the potential range of NDVI values for a given red reflectance was wider for lower reflectance. RadCaTS NDVI, while only with nadir measurements, showed the same trends as those of the satellites, validating the satellite results (Fig. 12j, m).

T-MODIS and A-MODIS EVIs decreased with increasing red reflectances nearly linearly (Fig. 12b, e). In contrast, VIIRS EVI increased with increasing red reflectances nearly linearly (Fig. 12h). RadCaTS EVIs only slightly increased with red reflectances, indicating their low sensitivity to the target brightness variations (Fig. 12k, n). The satellite EVIs, in particular, T-MODIS and A-MODIS, behaved differently from RadCaTS EVIs.

T-MODIS and A-MODIS EVI2s decreased with increasing red reflectances in the same manner as their respective EVIs (Fig. 12c, f). T-MODIS and A-MODIS EVI2 values were also nearly the same with their EVI counterparts. VIIRS EVI2 decreased very little with increasing red reflectances, being insensitive to the target brightness variations (Fig. 12i). RadCaTS EVI2 decreased with increasing red reflectances, but at lower rates than T-MODIS and A-MODIS EVI2. Compared with the EVI, the satellite EVI2 behaviors were comparable among the three satellite sensors and with the *in situ* counterparts.

Summarized in Table 8 are the mean VI and standard deviation values for this zero vegetation target, derived from all data. T-MODIS and A-MODIS VI mean values were comparable although A-MODIS VI mean values were slightly higher than the T-MODIS counterparts. S-VIIRS VI mean values were consistently higher than those of T-MODIS and A-MODIS.

5. Summary and discussions

In this study, the behavior of T-MODIS, A-MODIS, and S-VIIRS VIs was evaluated for zero vegetation conditions using the RRV playa, Nevada as the study site. The NDVI, EVI, and EVI2 were evaluated along with the input red, NIR, and blue reflectances. RadCaTS long-term, continuous *in situ* reflectance measurements, which were recently made available to the public *via* the RadCalNet portal (Bouvet et al., 2019), were used as a reference in evaluating the multi-sensor VIs and reflectances.

RadCaTS surface reflectance of the playa changed throughout seasons across years (0.3–0.45 for the red reflectance). T-MODIS, A-MODIS and S-VIIRS nadir/near-nadir reflectances captured these temporal variations well, having comparable temporal signatures to the RadCaTS counterparts. The satellite red and NIR reflectances were similar to or only slightly different from the RadCaTS counterparts, whereas T-MODIS and A-MODIS blue reflectances were lower than the RadCaTS counterparts (by ~0.05), and S-VIIRS blue reflectance was also lower than the RadCaTS counterpart by a smaller magnitude (~0.007).

RadCaTS NDVI, EVI, and EVI2 of the playa surface increased and decreased occasionally, but were reasonably constant for the time period examined in this study. These VI's temporal variations were less than the combined VI uncertainties propagated from the input reflectances. The satellite NDVI, EVI, and EVI2 had fairly flat temporal signatures, comparable to the RadCaTS counterparts. T-MODIS and A-MODIS NDVI and EVI2 values were comparable to the RadCaTS counterparts, whereas T-MODIS and A-MODIS EVI values were lower than the RadCaTS counterparts (*i.e.*, by ~0.006 and ~ 0.01 EVI units, respectively). All the three VIs of S-VIIRS were consistently higher than

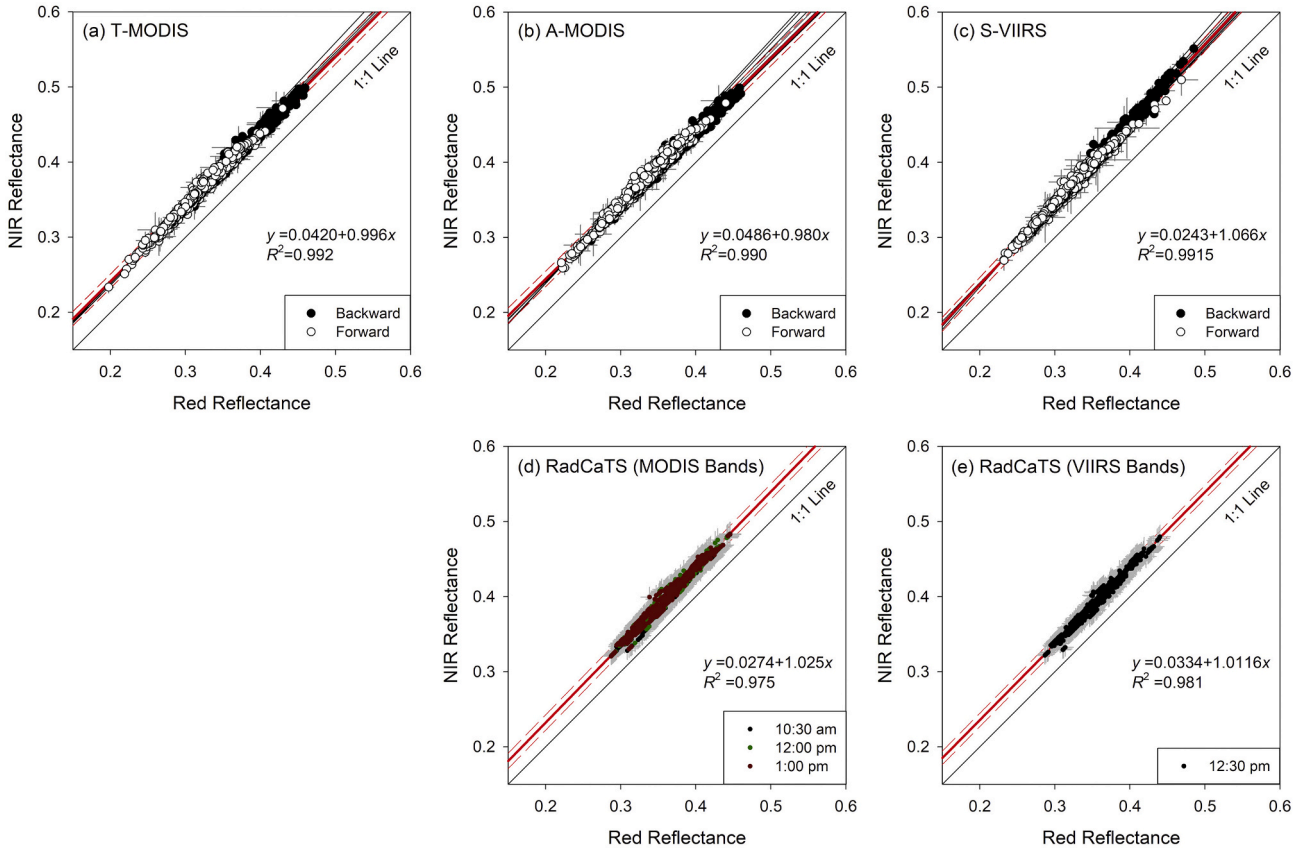

Fig. 10. NIR *vs.* red reflectance plots for (a) T-MODIS, (b) A-MODIS, (c) S-VIIRS, (d) RadCaTS band-averaged for MODIS bandpasses, and (e) RadCaTS band-averaged for VIIRS bandpasses. The thick and dashed red lines shown in individual plots are the regression lines and 95% prediction intervals derived using all data points on their corresponding plots. The thin black lines represent regression lines derived for individual view zenith angle bins. (For interpretation of the references to colour in this figure legend, the reader is referred to the web version of this article.)

their RadCaTS counterparts (*i.e.*, by ~0.008 VI units).

For this study site, the red and NIR, and red and blue reflectances each formed linear relationships (*i.e.*, soil lines) for each of the three sensors. Variations in reflectance due to surface conditions and observation geometries all appeared as variations along the same soil lines. Thus, off-nadir VIs were included to obtain the expected VI values and variations for zero vegetation conditions (Table 8), and the soil lines were used to systematically compare the behavior of the satellite VIs with the RadCaTS counterparts. Among the three indices examined in this study, the NDVI and EVI2 behaviors of all the three satellite sensors were comparable to their respective RadCaTS counterparts as well as among the three sensors. T-MODIS and A-MODIS EVIs behaved differently from the RadCaTS counterpart, whereas the S-VIIRS behavior was similar to the RadCaTS counterpart.

5.1. VI vs. reflectance errors

The satellite (including all of T-MODIS, A-MODIS, and S-VIIRS) *vs. in situ* reflectance differences for the red and NIR bands (0.01–0.015 level) obtained in this study were comparable to those reported by Vermote et al. (2014) who compared A-MODIS and S-VIIRS products with in-house, AERONET-corrected surface reflectance products. Our results of T-MODIS blue reflectance being lower than the *in situ* counterpart were also reported by Kharbouche et al. (2017) in their comparison results of T-MODIS reflectances with CAR-derived reflectances. In our results, A-MODIS blue reflectance was also lower than the *in situ* counterpart to the same degree with T-MODIS reflectance (*i.e.*, by ~0.05), and S-VIIRS blue reflectance was lower than the *in situ* counterpart, but to a less degree (*i.e.*, by ~0.007).

Positive validation results of individual band reflectances did not always translate into positive validation results of VIs computed from those reflectances. S-VIIRS reflectances had the smallest differences from the RadCaTS reflectances among the three sensors examined in this study. At the same time, S-VIIRS VIs (in particular the NDVI and EVI2) had the largest differences from the RadCaTS counterparts among the three sensors. Since S-VIIRS NIR reflectance was higher than the RadCaTS counterpart, whereas S-VIIRS and RadCaTS red reflectances were not different, the higher NIR reflectance led to the higher S-VIIRS VI values than the RadCaTS counterparts.

The reduced comparability of the satellite EVIs with the RadCaTS EVIs can be attributed to the blue band. For T-MODIS and A-MODIS EVIs, the lower blue reflectance made the EVI denominator higher, lowering the EVI values. Likewise, as shown in Fig. 11, the satellite blue-red reflectance relationships were different from those depicted by the *in situ* RadCaTS data. Our soil line analysis indicated that the different red-blue reflectance relationships were propagated into the slightly different EVI behaviors between the satellites and RadCaTS.

5.2. Long-term trends of playa reflectance

RadCaTS surface reflectance data indicated that the site reflectance decreased in the latter part of the year 2016, and remained lower for the rest of the study period. All the satellite reflectance data showed the same temporal patterns. We suspect that the white crust cover of the RadCaTS site slightly decreased in the year 2016, lowering the site reflectance after the event. According to the Blue Eagle Ranch weather station data, the playa experienced the largest winter snowfall in the 2016 winter during the study period along with the high rainfall that

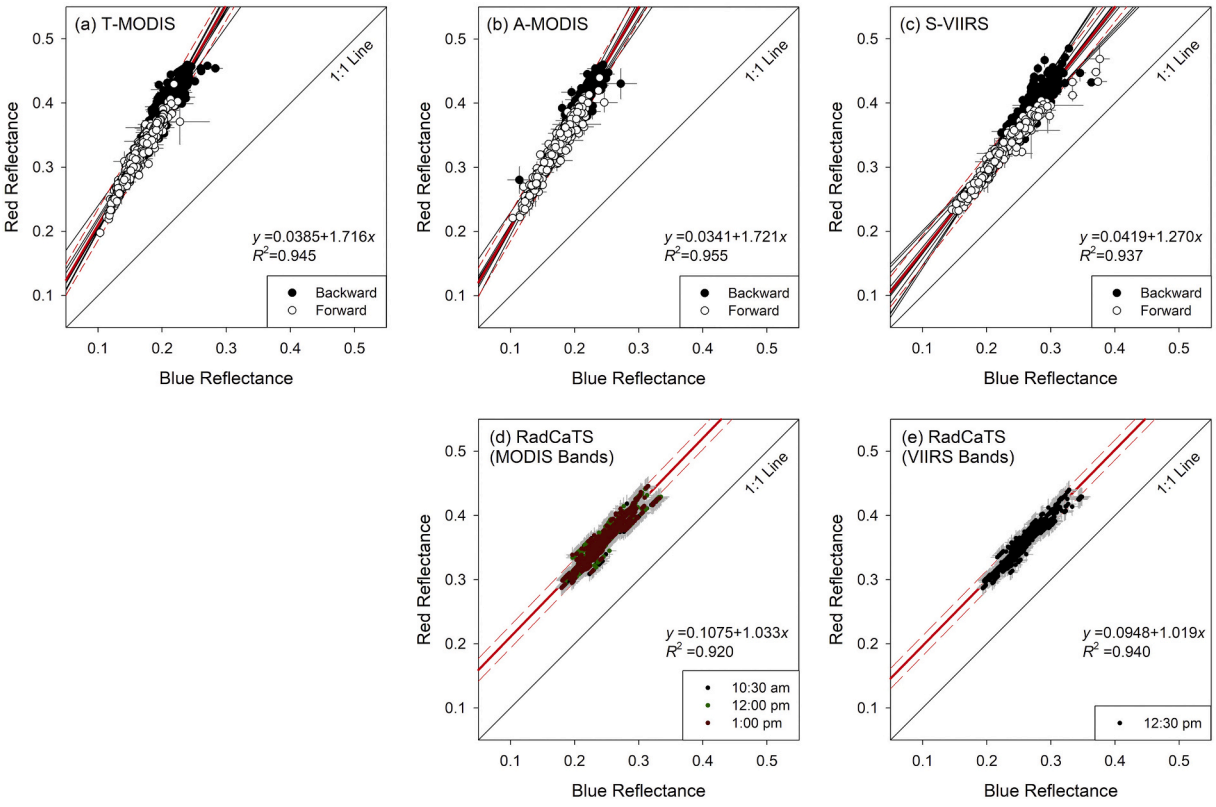

Fig. 11. Same as Fig. 10, but for red *vs.* blue reflectances. (For interpretation of the references to colour in this figure legend, the reader is referred to the web version of this article.)

continued throughout the 2016 spring (Fig. 3). These wet weather events might have reduced the white crust coverage. In the year 2020, the site reflectance increased again (Czapla-Myers, J., 2020, Unpublished results), indicating the dynamic nature of the site reflectance. Recently, digital cameras were installed for time-lapse photography of the RadCaTS site (Czapla-Myers, J., 2020, Personal communication). It is expected that the relationship between the site reflectance and surface condition (*e.g.*, white crust cover) will be understood better as the RadCaTS data continues to be collected for years to come.

It was only A-MODIS VIs that had increasing trends over the study period. An enhanced "response-*versus*-scan-angle (RVS)" calibration approach was applied to A-MODIS red, NIR, and blue bands only from 9 July 2016 onward, whereas the approach was implemented in T-MODIS red, NIR, and blue bands from 24 February 2000 onward (Bhatt et al., 2020). It is possible that this RVS calibration approach change did not affect the reflectance analysis results, but affected the trend analysis results of VIs derived from the reflectances. At the time of this writing, MODIS Collection 6.1 Land products are being generated where the enhanced RVS approach is applied to the entire A-MODIS data record (from 25 June 2002 onward).

5.3. Uncertainty of zero vegetation NDVI

The present study showed that the NDVI decreased with the soil brightness even for this single soil type. This indicates that the NDVI could falsely detect or miss the presence of green vegetation when a single NDVI value (*e.g.*, the mean, minimum, or maximum) was used to define the zero vegetation NDVI value even for the same soil background. For example, if the minimum NDVI value was used as a threshold, this NDVI-based vegetation detection would falsely inform the emergence of green vegetation or overestimate the green vegetation amount when the soil reflectance became lower due to the wetting of the soil surface or due to the forward scattering geometry (see Fig. 11). This will particularly be apparent in sparsely-vegetated areas or areas with intermediate vegetation cover as the contribution and influence of soil background reflectance to the top-of-canopy reflectance are significant in these areas (Privette et al., 1995). These results suggest to incorporate the soil brightness as an additional factor in determining the zero vegetation NDVI value to further reduce the uncertainty of the NDVI-based detection or quantification of biophysical parameters. Using nadir-BRDF-adjusted reflectances (*e.g.*, MCD43) in place of temporally-composited products (*e.g.*, MOD/MYD09 or MOD/MYD13) as the input reflectance source for VIs can reduce some of the soil brightness variations as the observation geometry is standardized to nadir viewing and, thus, reduce the uncertainty of the zero vegetation NDVI value.

5.4. Soil brightness effects on EVI

The EVI, that is a heritage of the soil-adjusted VI (SAVI), is designed to reduce the VI variations due to soil background brightness (Huete et al., 2002). This EVI characteristic can be demonstrated by the transformed soil line in the EVI-brightness space being parallel to the EVI isolines. RadCaTS EVIs showed this behavior where the data and soil lines were nearly parallel to the EVI isolines (Fig. 12k and n). For T-MODIS and A-MODIS EVIs, in contrast, the data and soil lines were not parallel to the EVI isolines, having their dependency to soil brightness. S-VIIRS EVI was less sensitive to soil background brightness variations, yet the projected soil line onto the EVI-brightness space had a steeper slope than the RadCaTS EVI counterpart. It is very likely that the negative bias in the blue reflectance impacted the EVI's ability to reduce the influence of soil brightness variations for T-MODIS and A-MODIS. For S-VIIRS EVI, it is not only the negative bias in the blue reflectance, but also the blue bandpass difference that contributed to this slightly-reduced EVI performance as the EVI coefficients optimized for the MODIS bandpasses were adopted for S-VIIRS. Obata et al. (2016) conducted a spectral cross-calibration experiment to derive a MODIS-compatible EVI from S-VIIRS

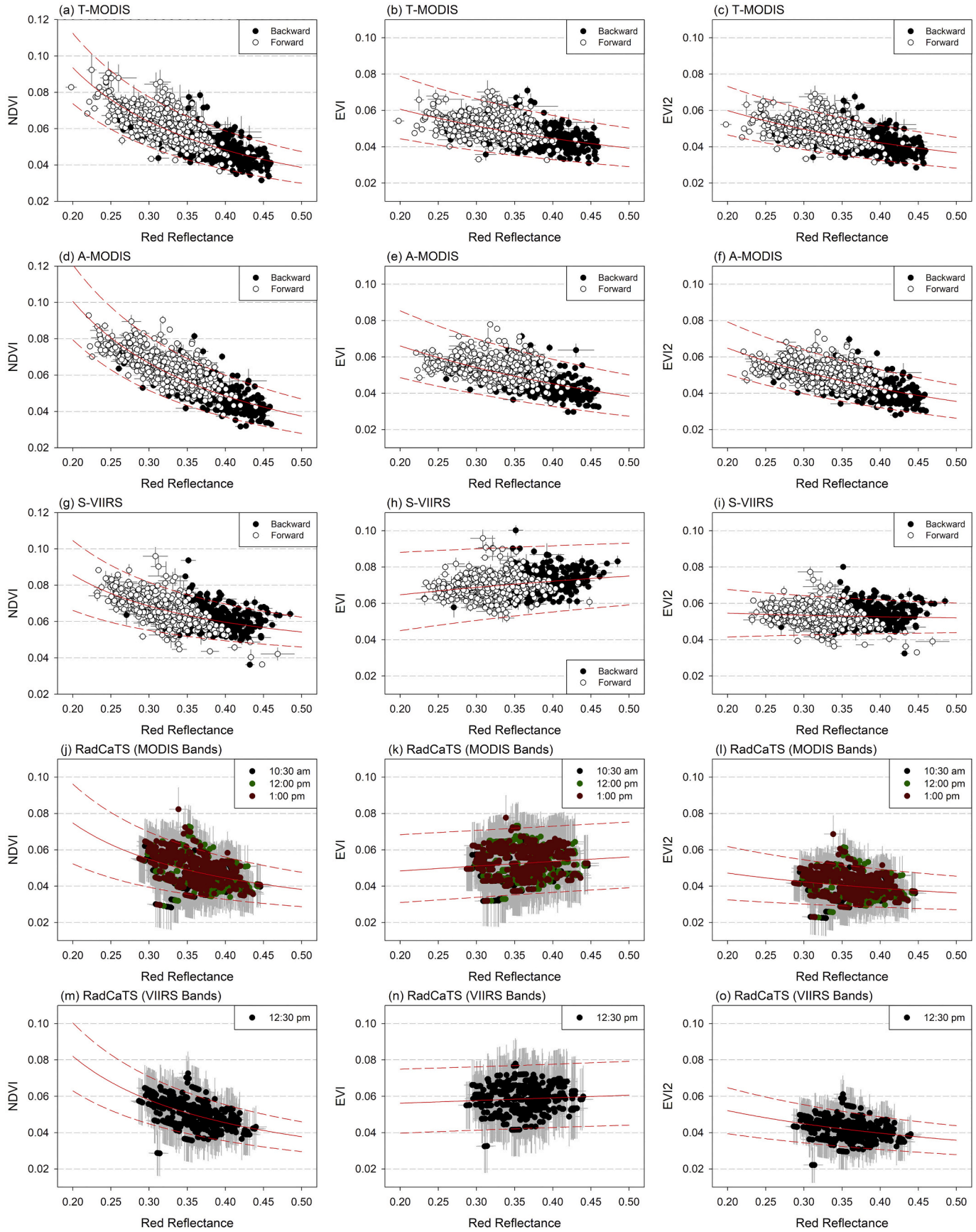

Fig. 12. VI *vs.* red reflectance plots. (For interpretation of the references to colour in this figure legend, the reader is referred to the web version of this article.)

Table 8
Summary statistics of satellite VIs for zero vegetation conditions represented by the RadCaTS site. The numbers in parentheses are standard deviations.

	NDVI	EVI	EVI2
T-MODIS	0.057 (0.010)	0.048 (0.006)	0.046 (0.007)
A-MODIS	0.058 (0.012)	0.050 (0.007)	0.048 (0.007)
S-VIIRS	0.065 (0.007)	0.070 (0.006)	0.053 (0.005)

reflectances using A-MODIS and S-VIIRS year-long global surface reflectance data. This cross-calibration exercise found an optimum C_2 coefficient value (see Eq. 4) to be ~6.5 which is lower than the current value of 7.5.

5.5. EVI-to-EVI2 consistency

T-MODIS and A-MODIS EVI2s did not normalize the soil brightness effect, *i.e.*, the transformed soil lines were not parallel to the EVI2 isolines. They behaved in the same way as their EVI counterparts, indicating excellent inter-VI compatibility. As described in Section 3.1, the EVI2 coefficients were determined for the optimum compatibility with the EVI for the MODIS bandpasses using actual MODIS surface reflectance data. RadCaTS EVI and EVI2 were different both in their values and in their behaviors, that is, the EVI and EVI2 soil lines were not parallel to each other. Interestingly, the S-VIIRS EVI and EVI2 soil lines were more comparable between them while their VI values were different.

Jiang et al. (2008) described that the optimization process can be considered as finding an appropriate blue-to-red reflectance ratio, and found 0.48 to be the optimum value for MODIS surface reflectance products [Jiang et al. (2008) actually obtained a red-to-blue reflectance ratio value, which was 2.08]. Here, the reflectance data in Fig. 12 were used to obtain the blue-to-red reflectance ratio. It was 0.52 for both T-MODIS and A-MODIS, but 0.68 for RadCaTS (MODIS). This supports that the current EVI2 coefficient is based on the relationship between the red and negatively-biased blue reflectances of MODIS. The blue-to-red reflectance ratio was 0.69 for S-VIIRS and 0.72 for RadCaTS (VIIRS).

Fensholt et al. (2006) reported the reduced cross-sensor compatibility of the EVI among T-MODIS, A-MODIS, MERIS, and VEGETATION, and attributed it to the different atmospheric correction schemes of the blue band. Given the highly sensitive blue band to the atmospheric correction scheme and the accurate atmospheric correction results achieved and demonstrated for the red and NIR reflectances, the choice of the EVI2 over the EVI is logical.

Similar VI validation exercises to this study (*i.e.*, using long-term *in situ* reflectance data as a reference) should be conducted for other bare soils to cover a range of soil brightness and types. They should also be performed for sparsely-to-intermediately vegetated areas where the soil background reflectance contributes to the top-of-canopy reflectance to examine how the soil lines and VI isolines align in the presence of green vegetation. It is important that these validation exercises not only evaluate VIs and input reflectances, but also the reflectance relationships across bands. The results of the present study suggest to re-optimize the EVI2 coefficients with *in situ* reflectance data first and then evaluate the applicability of the optimized coefficients with satellite data. Reliable optimization results of the EVI and EVI2 may only be achieved with a large number of validation results with long-term *in situ* reflectance data as a reference.

Declaration of Competing Interest

The authors declare that they have no known competing financial interests or personal relationships that could have appeared to influence the work reported in this paper.

Acknowledgements

The authors would like to thank Jeff Czapla-Myers for providing insightful information about the RadCaTS surface reflectance. The authors would also like to thank Yinphan Tsang for running the Mann-Kendall (MK) tests and assisting the interpretation of the MK test results. This work was supported by a NASA grant (80NSSC19K1691), a NOAA cooperative agreement (1333MD18PNEED0042), and JSPS KAKENHI grants (20 K20487 and 20 K12259).

Appendix I. Uncertainty Propagation Equations for Select Vegetation Indices

I.1. Enhanced Vegetation Index (EVI):

$$u^2(EVI) = \left(\frac{\partial EVI}{\partial \rho_{NIR}}\right)^2 u^2(\rho_{NIR}) + \left(\frac{\partial EVI}{\partial \rho_{red}}\right)^2 u^2(\rho_{red}) + \left(\frac{\partial EVI}{\partial \rho_{red}}\right)^2 u^2(\rho_{red}) + 2\frac{\partial EVI}{\partial \rho_{NIR}}\frac{\partial EVI}{\partial \rho_{red}} u(\rho_{NIR})u(\rho_{red})r_{NIR,red} + 2\frac{\partial EVI}{\partial \rho_{red}}\frac{\partial EVI}{\partial \rho_{blue}} u(\rho_{red})u(\rho_{blue})r_{red,blue} + 2\frac{\partial EVI}{\partial \rho_{blue}}\frac{\partial EVI}{\partial \rho_{NIR}} u(\rho_{blue})u(\rho_{NIR})r_{blue,NIR} \quad \text{(A1)}$$

where

$$\frac{\partial EVI}{\partial \rho_{\mathrm{NIR}}} = \frac{G[(1+C_1)\rho_{\mathrm{red}} - C_2\rho_{\mathrm{blue}} + L]}{(\rho_{\mathrm{NIR}} + C_1\rho_{\mathrm{red}} - C_2\rho_{\mathrm{blue}} + L)^2} \quad \text{(A2)}$$

$$\frac{\partial EVI}{\partial \rho_{\mathrm{red}}} = \frac{-G[(1+C_1)\rho_{\mathrm{NIR}} - C_2\rho_{\mathrm{blue}} + L]}{(\rho_{\mathrm{NIR}} + C_1\rho_{\mathrm{red}} - C_2\rho_{\mathrm{blue}} + L)^2} \quad \text{(A3)}$$

$$\frac{\partial EVI}{\partial \rho_{\mathrm{blue}}} = \frac{GC_2(\rho_{\mathrm{NIR}} - \rho_{\mathrm{red}})}{(\rho_{\mathrm{NIR}} + C_1\rho_{\mathrm{red}} - C_2\rho_{\mathrm{blue}} + L)^2} \quad \text{(A4)}$$

I.2. Two-band, Enhanced Vegetation Index (EVI2):

$$u^2(EVI2) = \left(\frac{\partial EVI2}{\partial \rho_{NIR}}\right)^2 u^2(\rho_{NIR}) + \left(\frac{\partial EVI2}{\partial \rho_{red}}\right)^2 u^2(\rho_{red}) + 2\frac{\partial EVI2}{\partial \rho_{NIR}}\frac{\partial EVI2}{\partial \rho_{red}} u(\rho_{NIR})u(\rho_{red})r_{NIR,red} \quad \text{(A5)}$$

where

$$\frac{\partial EVI2}{\partial \rho_{\mathrm{NIR}}} = \frac{2.5(3.4\rho_{\mathrm{red}} + 1)}{(\rho_{\mathrm{NIR}} + 2.4\rho_{\mathrm{red}} + 1)^2} \quad \text{(A6)}$$

$$\frac{\partial EVI2}{\partial \rho_{\mathrm{red}}} = \frac{-2.5(3.4\rho_{\mathrm{NIR}} + 1)}{(\rho_{\mathrm{NIR}} + 2.4\rho_{\mathrm{red}} + 1)^2} \quad \text{(A7)}$$

References

Badgley, G., Field, C.B., Berry, J.A., 2017. Canopy near-infrared reflectance and terrestrial photosynthesis. Sci. Adv. 3, e1602244 https://doi.org/10.1126/sciadv.1602244.

Barbosa, H.A., Lakshmi Kumar, T.V., Paredes, F., Elliott, S., Ayuga, J.G., 2019. Assessment of Caatinga response to drought using Meteosat-SEVIRI normalized difference vegetation index (2008-2016). ISPRS J. Photogramm. Remote Sens. 148, 235–252. https://doi.org/10.1016/j.isprsjprs.2018.12.014.

Baret, F., Jacquemoud, S., Hanocq, J.F., 1993. About the soil line concept in remote sensing. Adv. Space Res. 13 (5), 281–284. https://doi.org/10.1016/0273-1177(93)90560-X.

Bhatt, R., Doelling, D.R., Angal, A., Xiong, X., Haney, C., Scarino, B.R., Gopalan, A., 2020. Response versus scan-angle assessment of MODIS reflective solar bands in Collection 6.1 calibration. IEEE Transactions on Geoscience and Remote Sensing 58 (4), 2276–2289. https://doi.org/10.1109/TGRS.2019.2946963.

Bhimala, K.R., Rakesh, V., Prasad, K.R., Mohapatra, G.N., 2020. Identification of vegetation responses to soil moisture, rainfall, and LULC over different meteorological subdivisions in India using remote sensing data. Theor. Appl. Climatol. 142 (3), 987–1001. https://doi.org/10.1007/s00704-020-03360-8.

Bolton, D.K., Gray, J.M., Melaas, E.K., Moon, M., Eklundh, L., Friedl, M.A., 2020. Continental-scale land surface phenology from harmonized Landsat 8 and Sentinel-2 imagery. Remote Sens. Environ. 240, 111685. https://doi.org/10.1016/j.rse.2020.111685.

Bouvet, M., Thome, K., Berthelot, B., Bialek, A., Czapla-Myers, J., Fox, P.N., Woolliams, R.E., 2019. RadCalNet: A radiometric calibration network for earth observing imagers operating in the visible to shortwave infrared spectral range. Remote Sensing 11 (20), 2401. https://doi.org/10.3390/rs11202401.

Bruegge, C.J., Coburn, C., Elmes, A., Helmlinger, M.C., Kataoka, F., Kuester, M., Schwandner, F.M., 2019. Bi-directional reflectance factor determination of the Railroad Valley playa. Remote Sensing 11 (22), 2601. https://doi.org/10.3390/rs11222601.

Campbell, P.K.E., Middleton, E.M., Thome, K.J., Kokaly, R.F., Huemmrich, K.F., Lagomasino, D., Brunsell, N.A., 2013. EO-1 Hyperion reflectance time series at calibration and validation sites: Stability and sensitivity to seasonal dynamics. IEEE J. Select. Top. Appl. Earth Observ.Remote Sens. 6 (2), 276–290. https://doi.org/10.1109/JSTARS.2013.2246139.

Cao, C., DeLuccia, F.J., Xiong, X., Wolfe, R., Weng, F., 2014. Early on-orbit performance of the visible infrared imaging radiometer suite onboard the Suomi National Polar-Orbiting Partnership (S-NPP) satellite. IEEE Trans. Geosci. Remote Sens. 52 (2), 1142–1156. https://doi.org/10.1109/TGRS.2013.2247768.

Cheng, Y., Gamon, J.A., Fuentes, D.A., Mao, Z., Sims, D.A., Qiu, H.-L., Rahman, A.F., 2006. A multi-scale analysis of dynamic optical signals in a Southern California chaparral ecosystem: a comparison of field, AVIRIS and MODIS data. Remote Sens. Environ. 103 (3), 369–378. https://doi.org/10.1016/j.rse.2005.06.013.

Cho, M.A., Ramoelo, A., 2019. Optimal dates for assessing long-term changes in tree-cover in the semi-arid biomes of South Africa using MODIS NDVI time series (2001-2018). Int. J. Appl. Earth Obs. Geoinf. 81, 27–36. https://doi.org/10.1016/j.jag.2019.05.014.

Core Team, R., 2020. R: A Language and Environment for Statistical Computing. R Foundation for Statistical Computing, Vienna, Austria. Retrieved from. https://www.R-project.org/.

Czapla-Myers, J., 2018. RadCalNet Site Description: Railroad Valley, USA (QA4EO-WGCV-IVO-CSP-002_RVUS).

Czapla-Myers, J., Woolliams, E., 2018. Uncertainty analysis statement - RVUS. In: RadCalNet Uncertainty Statement, QA4EO-WGCV-IVO-CSP-002, 7p.

Czapla-Myers, J.S., Thome, K.J., Buchanan, J.H., 2007. Implication of spatial uniformity on vicarious calibration using automated test sites. In: Proc. SPIE 6677, Earth Observing Systems XII, 66770U. https://doi.org/10.1117/12.732661.

Czapla-Myers, J.S., Thome, K.J., Cocilovo, B.R., McCorkel, J.T., Buchanan, J.H., 2008. Temporal, spectral, and spatial study of the automated vicarious calibration test site at Railroad Valley, Nevada. In: Proc. SPIE 7081, Earth Observing Systems XIII, 70810I. https://doi.org/10.1117/12.795551.

Czapla-Myers, J., Ong, L., Thome, K., McCorkel, J., 2016. Validation of EO-1 Hyperion and advanced land imager using the radiometric calibration test site at Railroad Valley, Nevada. IEEE J. Select. Top. Appl. Earth Observ.Remote Sens. 9 (2), 816–826. https://doi.org/10.1109/JSTARS.2015.2463101.

Czapla-Myers, J., McCorkel, J., Anderson, N., Biggar, S., 2017. Earth-observing satellite intercomparison using the radiometric calibration test site at Railroad Valley. J. Appl. Remote. Sens. 12 (1), 012004 https://doi.org/10.1117/1.JRS.12.012004.

Didan, K., Barreto Munez, A., Tucker, C.J., Pinzon, E.J., 2018. Suomi National Polar-Orbiting Partnership Visible Infrared Imaging Radiometer Suite Vegetation Index Product Suite User Guide and Abridged Algorithm Theoretical Basis Document. The University of Arizona.

Fensholt, R., Sandholt, I., Rasmussen, M.S., 2004. Evaluation of MODIS LAI, fAPAR and the relation between fAPAR and NDVI in a semi-arid environment using in situ measurements. Remote Sens. Environ. 91 (3–4), 490–507. https://doi.org/10.1016/j.rse.2004.04.009.

Fensholt, R., Sandholt, I., Stisen, S., 2006. Evaluating MODIS, MERIS, and VEGETATION - VEGETATION indices using in situ measurements in a semiarid environment. IEEE Trans. Geosci. Remote Sens. 44 (7), 1774–1786. https://doi.org/10.1109/TGRS.2006.875940.

Fox, G.A., Sabbagh, G.J., Searcy, S.W., Yang, C., 2004. An automated soil line identification routine for remotely sensed images. Soil Sci. Soc. Am. J. 68 (4), 1326–1331. https://doi.org/10.2136/sssaj2004.1326.

Galvão, L.S., Vitorello, Í., 1998. Variability of laboratory measured soil lines of soils from southeastern Brazil. Remote Sens. Environ. 63 (2), 166–181. https://doi.org/10.1016/S0034-4257(97)00135-1.

Gitelson, A.A., Peng, Y., Huemmrich, K.F., 2014. Relationship between fraction of radiation absorbed by photosynthesizing maize and soybean canopies and NDVI from remotely sensed data taken at close range and from MODIS 250 m resolution data. Remote Sens. Environ. 147, 108–120. https://doi.org/10.1016/j.rse.2014.02.014.

Gutman, G., Ignatov, A., 1998. The derivation of the green vegetation fraction from NOAA/AVHRR data for use in numerical weather prediction models. Int. J. Remote Sens. 19 (8), 1533–1543. https://doi.org/10.1080/014311698215333.

Hipel, K.W., McLeod, A.I., 1994. Time Series Modelling of Water Resources and Environmental Systems. Elsevier Science.

Huete, A.R., 1989. Soil influences in remotely sensed vegetation-canopy spectra. In: Asrar, G. (Ed.), Theory and Applications of Optical Remote Sensing, pp. 107–141.

Huete, A., Didan, K., Miura, T., Rodriguez, E.P., Gao, X., Ferreira, L.G., 2002. Overview of the radiometric and biophysical performance of the MODIS vegetation indices. Remote Sens. Environ. 83 (1–2), 195–213. https://doi.org/10.1016/S0034-4257(02)00096-2.

Ichii, K., Matsui, Y., Yamaguchi, Y., Ogawa, K., 2001. Comparison of global net primary production trends obtained from satellite-based normalized difference vegetation index and carbon cycle model. Glob. Biogeochem. Cycles 15 (2), 351–363. https://doi.org/10.1029/2000GB001296.

Irons, J.R., Campbell, G.S., Norman, J.M., Graham, D.W., Kovalick, W.M., 1992. Prediction and measurement of soil bidirectional reflectance. IEEE Trans. Geosci. Remote Sens. 30 (2), 249–260. https://doi.org/10.1109/36.134075.

Jackson, J.M., Liu, H., Laszlo, I., Kondragunta, S., Remer, L.A., Huang, J., Huang, H.-C., 2013. Suomi-NPP VIIRS aerosol algorithms and data products. J. Geophys. Res. - Atmos. 118 (22), 12,673–12,689. https://doi.org/10.1002/2013JD020449.

Jiang, Z., Huete, A.R., Didan, K., Miura, T., 2008. Development of a two-band enhanced vegetation index without a blue band. Remote Sens. Environ. 112 (10), 3833–3845. https://doi.org/10.1016/j.rse.2008.06.006.

Kaufman, Y.J., Tanré, D., Remer, L.A., Vermote, E.F., Chu, A., Holben, B.N., 1997. Operational remote sensing of tropospheric aerosol over land from EOS moderate resolution imaging spectroradiometer. J. Geophys. Res. 102 (D14), 17051–17067. Retrieved from. https://doi.org/10.1029/96JD03988.

Kendall, M.G., 1975. Rank Correlation Methods, 4th ed. Charles Griffin, London, U.K.

Kharbouche, S., Muller, J.-P., Gatebe, C.K., Scanlon, T., Banks, A.C., 2017. Assessment of satellite-derived surface reflectances by NASA's CAR airborne radiometer over Railroad Valley Playa. Remote Sensing 9 (6), 562. https://doi.org/10.3390/rs9060562.

Liang, L., Schwartz, M.D., Fei, S., 2011. Validating satellite phenology through intensive ground observation and landscape scaling in a mixed seasonal forest. Remote Sens. Environ. 115 (1), 143–157. https://doi.org/10.1016/j.rse.2010.08.013.

Liang, L., Schwartz, M.D., Wang, Z., Gao, F., Schaaf, C.B., Tan, B., Zhang, X., 2014. A cross comparison of spatiotemporally enhanced springtime phenological measurements from satellites and ground in a northern U.S. mixed forest. IEEE Transactions on Geoscience and Remote Sensing 52 (12), 7513–7526. https://doi.org/10.1109/TGRS.2014.2313558.

Libiseller, C., Grimvall, A., 2002. Performance of partial Mann-Kendall tests for trend detection in the presence of covariates. Environmetrics 13 (1), 71–84. https://doi.org/10.1002/env.507.

Liu, L., Xiao, X., Qin, Y., Wang, J., Xu, X., Hu, Y., Qiao, Z., 2020. Mapping cropping intensity in China using time series Landsat and Sentinel-2 images and Google Earth Engine. Remote Sens. Environ. 239, 111624. https://doi.org/10.1016/j.rse.2019.111624.

Lu, J., Carbone, G.J., Gao, P., 2019. Mapping the agricultural drought based on the long-term AVHRR NDVI and North American Regional Reanalysis (NARR) in the United States, 1981-2013. Appl. Geogr. 104, 10–20. https://doi.org/10.1016/j.apgeog.2019.01.005.

Matsui, T., Lakshmi, V., Small, E.E., 2005. The effects of satellite-derived vegetation cover variability on simulated land-atmosphere interactions in the NAMS. J. Clim. 18 (1), 21–40. https://doi.org/10.1175/JCLI3254.1.

Miura, T., Yoshioka, H., 2018. Hyperspectral data in long-term, cross-sensor continuity studies (Chapter 13). In: Thenkabail, P.S., Lyon, J.G., Huete, A. (Eds.), Advanced Applications in Remote Sensing of Agricultural Crops and Natural Vegetation, 2nd Ed. CRC Press, Taylor and Francis Group. https://doi.org/10.1201/9780429431166.

Miura, T., Huete, A.R., Yoshioka, H., 2000. Evaluation of sensor calibration uncertainties on vegetation indices for MODIS. IEEE Trans. Geosci. Remote Sens. 38 (3), 1399–1409. https://doi.org/10.1109/36.843034.

Miura, T., Nagai, S., Takeuchi, M., Ichii, K., Yoshioka, H., 2019. Improved characterisation of vegetation and land surface seasonal dynamics in Central Japan with Himawari-8 hypertemporal data. Sci. Rep. 9 (1), 15692. https://doi.org/10.1038/s41598-019-52076-x.

MODIS Characterization Support Team, 2020. Calibration Section - Parameters. https://mcst.gsfc.nasa.gov/calibration/parameters (accessed 19 October 2020).

Montandon, L.M., Small, E.E., 2008. The impact of soil reflectance on the quantification of the green vegetation fraction from NDVI. Remote Sens. Environ. 112 (4), 1835–1845. https://doi.org/10.1016/j.rse.2007.09.007.

Muraoka, H., Noda, H.M., Nagai, S., Motohka, T., Saitoh, T.M., Nasahara, K.N., Saigusa, N., 2013. Spectral vegetation indices as the indicator of canopy photosynthetic productivity in a deciduous broadleaf forest. J. Plant Ecol. 6 (5), 393–407. https://doi.org/10.1093/jpe/rts037.

NOAA STAR Calibration Center, 2017. VIIRS relative spectral response function (RSR). https://ncc.nesdis.noaa.gov/VIIRS/VIIRSSpectralResponseFunctions.php.

Obata, K., Miura, T., Yoshioka, H., Huete, A., Vargas, M., 2016. Spectral cross-calibration of VIIRS enhanced vegetation index with MODIS: a case study using year-long global data. Remote Sens. 8 (1), 34. https://doi.org/10.3390/rs8010034.

Obata, K., Tsuchida, S., Yamamoto, H., Thome, K., 2017. Cross-calibration between ASTER and MODIS visible to near-infrared bands for improvement of ASTER radiometric calibration. Sensors 17 (8), 1793. https://doi.org/10.3390/s17081793.

Olofsson, P., Lagergren, F., Lindroth, A., Lindstrom, J., Klemedtsson, L., Kutsch, W., Eklundh, L., 2008. Towards operational remote sensing of forest carbon balance across northern Europe. Biogeosciences 5 (3), 817–832.

Pohlert, T., 2020. trend: Non-Parametric Trend Tests and Change-Point Detection. R package version 1.1.4. Retrieved from. https://CRAN.R-project.org/package=trend.

Privette, J.L., Myneni, R.B., Emery, W.J., Pinty, B., 1995. Inversion of a soil bidirectional reflectance model for use with vegetation reflectance models. J. Geophys. Res. 100 (D12), 25497–25508. https://doi.org/10.1029/95JD00851.

Qiao, K., Zhu, W., Xie, Z., 2020. Application conditions and impact factors for various vegetation indices in constructing the LAI seasonal trajectory over different vegetation types. Ecol. Indic. 112, 106153. https://doi.org/10.1016/j.ecolind.2020.106153.

Rankine, C., Sanchez-Azofeifa, G.A., Guzman, J.A., Espirito-Santo, M.M., Sharp, I., 2017. Comparing MODIS and near-surface vegetation indexes for monitoring tropical dry forest phenology along a successional gradient using optical phenology towers. Environ. Res. Lett. 12 (10), 105007. https://doi.org/10.1088/1748-9326/aa838c.

Seddon, A.W.R., Macias-Fauria, M., Long, P.R., Benz, D., Willis, K.J., 2016. Sensitivity of global terrestrial ecosystems to climate variability. Nature 531 (7593), 229–232. https://doi.org/10.1038/nature16986.

Shi, H., Li, L., Eamus, D., Huete, A., Cleverly, J., Tian, X., Carrara, A., 2017. Assessing the ability of MODIS EVI to estimate terrestrial ecosystem gross primary production of multiple land cover types. Ecological Indicators 72, 153–164. https://doi.org/10.1016/j.ecolind.2016.08.022.

Taylor, B.N., Kuyatt, C.E., 2007. Guidelines for Evaluating and Expressing the Uncertainty of NIST Measurement Results, [Online]. National Institute of Standards and Technology, Gaithersburg, Maryland, USA. http://physics.nist.gov/TN1297 (accessed 23 April 2020).

Teillet, P.M., Markham, B.L., Irish, R.R., 2006. Landsat cross-calibration based on near simultaneous imaging of common ground targets. Remote Sens. Environ. 102 (3–4), 264–270. https://doi.org/10.1016/j.rse.2006.02.005.

Teillet, P.M., Fedosejevs, G., Thome, K.J., Barker, J.L., 2007. Impacts of spectral band difference effects on radiometric cross-calibration between satellite sensors in the solar-reflective spectral domain. Remote Sens. Environ. 110 (3), 393–409. https://doi.org/10.1016/j.rse.2007.03.003.

Vargas, M., Miura, T., Shabanov, N., Kato, A., 2013. An initial assessment of Suomi NPP VIIRS vegetation index EDR. J. Geophys. Res.-Atmos. 118 (22), 12,301–12,316. https://doi.org/10.1002/2013JD020439.

Vermote, E.F., Kotchenova, S., 2008. Atmospheric correction for the monitoring of land surfaces. J. Geophys. Res. 113 (D23S90) https://doi.org/10.1029/2007JD009662. Retrieved from.

Vermote, E.F., Saleous, N.Z., 2006. Operational atmospheric correction of MODIS visible to middle infrared land surface data in the case of an infinite Lambertian target. In: J. J. Q. E. Al. (Ed.), Earth Science Satellite Remote Sensing, Science and Instruments, Volume 1. Tsinghua UnivPress, Beijing, pp. 123–153.

Vermote, E., Wolfe, R., 2015a. MOD09GA MODIS/Terra surface reflectance daily L2G global 1km and 500m SIN grid V006. In: NASA EOSDIS Land Processes DAAC. https://doi.org/10.5067/MODIS/MOD09GA.006 (accessed 8 July 2020).

Vermote, E., Wolfe, R., 2015b. MYD09GA MODIS/aqua surface reflectance daily L2G global 1km and 500m SIN grid V006. In: NASA EOSDIS Land Processes DAAC. https://doi.org/10.5067/MODIS/MYD09GA.006 (accessed 10 July 2020.

Vermote, E., Justice, C., Csiszar, I., 2014. Early evaluation of the VIIRS calibration, cloud mask and surface reflectance earth data records. Remote Sens. Environ. 148 (Supplement C), 134–145. https://doi.org/10.1016/j.rse.2014.03.028.

Wang, Q., Tenhunen, J., Dinh, N.Q., Reichstein, M., Vesala, T., Keronen, P., 2004. Similarities in ground- and satellite-based NDVI time series and their relationship to physiological activity of a scots pine forest in Finland. Remote Sens. Environ. 93 (1–2), 225–237. https://doi.org/10.1016/j.rse.2004.07.006.

Wang, Y., Czapla-Myers, J., Lyapustin, A., Thome, K., Dutton, E.G., 2011. AERONET-based surface reflectance validation network (ASRVN) data evaluation: case study for railroad valley calibration site. Remote Sens. Environ. 115 (10), 2710–2717. https://doi.org/10.1016/j.rse.2011.06.011.

Wang, Z., Coburn, C.A., Ren, X., Teillet, P.M., 2014. Effect of surface roughness, wavelength, illumination, and viewing zenith angles on soil surface BRDF using an imaging BRDF approach. Int. J. Remote Sens. 35 (19), 6894–6913. https://doi.org/10.1080/01431161.2014.960616.

Wolfe, R.E., Roy, D.P., Vermote, E., 1998. MODIS land data storage, gridding, and compositing methodology: level 2 grid. IEEE Trans. Geosci. Remote Sens. 36 (4), 1324–1338.

Wolfe, R.E., Nishihama, M., Fleig, A.J., Kuyper, J.A., Roy, D.P., Storey, J.C., Patt, F.S., 2002. Achieving sub-pixel geolocation accuracy in support of MODIS land science. Remote Sens. Environ. 83 (1–2), 31–49. https://doi.org/10.1016/S0034-4257(02)00085-8.

Wolfe, R.E., Lin, G., Nishihama, M., Tewari, K.P., Tilton, J.C., Isaacman, A.R., 2013. Suomi NPP VIIRS prelaunch and on-orbit geometric calibration and characterization. J. Geophys. Res. - Atmos. 118 (20), 11,508–11,521. https://doi.org/10.1002/jgrd.50873.

Wu, D., Wu, H., Zhao, X., Zhou, T., Tang, B., Zhao, W., Jia, K., 2014. Evaluation of spatiotemporal variations of global fractional vegetation cover based on GIMMS NDVI data from 1982 to 2011. Remote Sens. 6 (5), 4217–4239. https://doi.org/10.3390/rs6054217.

Yan, K., Park, T., Yan, G., Liu, Z., Yang, B., Chen, C., Myneni, R.B., 2016. Evaluation of MODIS LAI/FPAR product Collection 6. Part 2: Validation and intercomparison. Remote Sens. *8* (6), 460. https://doi.org/10.3390/rs8060460.

Yan, D., Zhang, X., Nagai, S., Yu, Y., Akitsu, T., Nasahara, K.N., Maeda, T., 2019. Evaluating land surface phenology from the Advanced Himawari Imager using observations from MODIS and the Phenological Eyes Network. International Journal of Applied Earth Observation and Geoinformation 79, 71–83. https://doi.org/10.1016/j.jag.2019.02.011.

Yates, E.L., Detweiler, A.M., Iraci, L.T., Bebout, B.M., McKay, C.P., Schiro, K., Loewenstein, M., 2013. Assessing the role of alkaline soils on the carbon cycle at a playa site. Environmental Earth Sciences 70 (3), 1047–1056. https://doi.org/10.1007/s12665-012-2194-x.

Yoshioka, H., Miura, T., Demattê, J.A.M., Batchily, K., Huete, A.R., 2010. Soil line influences on two-band vegetation indices and vegetation isolines: a numerical study. Remote Sens. 2 (2), 545–561. Retrieved from. http://www.mdpi.com/2072-4292/2/2/545.

Zeng, X., Dickinson, R.E., Walker, A., Shaikh, M., DeFries, R.S., Qi, J., 2000. Derivation and evaluation of global 1-km fractional vegetation cover data for land modeling. J. Appl. Meteorol. 39 (6), 826–839. https://doi.org/10.1175/1520-0450(2000)039<0826:DAEOGK>2.0.CO;2.

Zhang, Y., Song, C., Band, L.E., Sun, G., Li, J., 2017. Reanalysis of global terrestrial vegetation trends from MODIS products: Browning or greening. Remote Sens. Environ. 191, 145–155. https://doi.org/10.1016/j.rse.2016.12.018.

Zhu, Z., Fu, Y., Woodcock, C.E., Olofsson, P., Vogelmann, J.E., Holden, C., Yu, Y., 2016. Including land cover change in analysis of greenness trends using all available Landsat 5, 7, and 8 images: A case study from Guangzhou, China (2000-2014). Remote Sensing of Environment 185, 243–257. https://doi.org/10.1016/j.rse.2016.03.036.